

# Benchmarking the simulation of Cr isotope fractionation

Christoph Wanner · Jennifer L. Druhan ·  
Richard T. Amos · Peter Alt-Epping ·  
Carl I. Steefel

Received: 31 January 2014 / Accepted: 27 June 2014 / Published online: 1 August 2014  
© Springer International Publishing Switzerland 2014

**Abstract** A benchmark problem set consisting of four problem levels was developed for the simulation of Cr isotope fractionation in 1D and 2D domains. The benchmark is based on a recent field study where Cr(VI) reduction and accompanying Cr isotope fractionation occurs abiotically by an aqueous reaction with dissolved  $\text{Fe}^{2+}$  (Wanner et al., 2012., Appl. Geochem., 27, 644–662). The problem set includes simulation of the major processes affecting the Cr isotopic composition such as the dissolution of various Cr(VI) bearing minerals, fractionation during abiotic aqueous Cr(VI) reduction, and non-fractionating precipitation of Cr(III) as sparingly soluble Cr-hydroxide.

Accuracy of the presented solutions was ensured by running the problems with four well-established reactive transport modeling codes: TOUGHREACT, MIN3P, CRUNCHFLOW, and FLOTRAN. Results were also compared with

an analytical Rayleigh-type fractionation model. An additional constraint on the correctness of the results was obtained by comparing output from the problem levels simulating Cr isotope fractionation with the corresponding ones only simulating bulk concentrations. For all problem levels, model to model comparisons showed excellent agreement, suggesting that for the tested geochemical processes any code is capable of accurately simulating the fate of individual Cr isotopes.

**Keywords** Reactive transport modeling · Benchmark · Cr reduction · Cr isotopes · Remediation

## 1 Introduction

Chromium(VI) is a serious (e.g., carcinogenic) inorganic contaminant [1] released by anthropogenic activities (e.g., galvanization) as well as from geogenic sources such as oxidative weathering of ultramafic rocks [2]. In contrast, the reduced chromium form, Cr(III), is less toxic [3], sparingly soluble, adsorbs strongly on solid surfaces, and co-precipitates with Fe(III) hydroxides [4, 5]. Reduction of Cr(VI) to Cr(III) is therefore a desirable method for remediation of Cr(VI) contaminated sites. Chromium(VI) reduction either occurs naturally by the presence of organic carbon or  $\text{Fe}^{2+}$  bearing minerals [6], or by the implementation of in situ remediation measures where organic or inorganic Cr reductants are injected into the aquifer [7–11].

The fractionation of stable Cr isotopes has become a well-accepted proxy for demonstrating Cr(VI) reduction in experimental [12–15] and natural systems [9, 16–19]. These studies generally show that of the prevalent naturally occurring Cr isotopes, the heavier  $^{53}\text{Cr}$  accumulates in the unreacted Cr(VI) pool and the lighter  $^{52}\text{Cr}$  preferentially

---

**Electronic supplementary material** The online version of this article (doi:10.1007/s10596-014-9436-9) contains supplementary material, which is available to authorized users.

---

C. Wanner (✉) · C. I. Steefel  
Earth Sciences Division, Lawrence Berkeley National Laboratory,  
1 Cyclotron Road, Berkeley, CA, 94720, USA  
e-mail: cwanner@lbl.gov

J. L. Druhan  
Department of Geological and Environmental Sciences,  
Stanford University, Stanford, CA, 94305, USA

R. T. Amos  
Department of Earth and Environmental Sciences,  
University of Waterloo, Waterloo, Ontario, Canada

P. Alt-Epping  
Institute of Geological Sciences, University of Bern,  
Bern, Switzerland

reacts to form Cr(III). In contrast, Cr(III) did not exhibit kinetic isotope discrimination during a Cr(III) oxidation experiment [12]. Cr isotopic fractionation is typically explained with kinetic Rayleigh-type fractionation models because once reduced, Cr precipitates as Cr(III) hydroxides or adsorbs on solid surfaces and thus no longer interacts with the remaining soluble Cr(VI). Ideally such Rayleigh-type models can be applied for natural systems to infer the extent of Cr(VI) reduction assuming that the isotopic fractionation factor is known [20]. This assumption is, however, challenging because various published Cr(VI) reduction experiments have shown that field-scale effective fractionation factors may vary over a broad range (see compilation by Wanner and Sonnenthal [21]). Discrepancies in observed Cr isotopic fractionation factors have been attributed to variable kinetic and transport effects as well as different reaction mechanisms [12, 17, 21–23]. Studies for other isotopic systems confirmed that effective fractionation factors vary for a single reaction mechanism due to varying precipitation rates (e.g., Ca [24, 25]) and/or varying hydrodynamic dispersion (e.g., N, C, [26–28]). The broad range of observed fractionation factors and their dependence on transport and kinetic processes may often require the use of reactive transport modeling for the quantitative interpretation of field scale Cr isotope data.

To date, reactive transport modeling involving Cr isotope fractionation has only been applied in a few selected field and lab studies [21, 29, 30]. Other studies have employed numerical reactive transport codes to simulate isotopic fractionation for other contaminated systems, including sulfur isotopic fractionation during sulfate reduction [31, 32, 34] and carbon and chlorine isotopic fractionation during degradation of organic contaminants [35–40].

The cited isotope modeling studies employ different approaches for simulating aqueous kinetic isotope fractionation. To test the different approaches, this paper aims to provide a benchmark problem set for the simulation of Cr isotope fractionation during aqueous kinetic Cr(VI) reduction. Further, the benchmark tests the simulation of other fundamental geochemical processes that define the fate of individual Cr isotopes. Evaluated processes include non-fractionating Cr(III) precipitation and dissolution of Cr(VI)-bearing minerals in addition to Cr isotope fractionation during aqueous kinetic Cr(VI) reduction. The benchmark problem is largely adapted from an extended field and modeling study of an actual Cr(VI) contaminated site located in Switzerland, where Cr(VI) reduction occurs naturally and where monitored natural attenuation (MNA) is part of the remediation measures [18, 30]. To ensure that results presented here provide accurate simulation results, four different multicomponent reactive transport codes have been used to simulate this problem set. These codes are TOUGHREACT, MIN3P, FLOTRAN, and CRUNCHFLOW. General

capabilities and numerical model formulations of these codes are provided in Steefel et al. [41] and references therein.

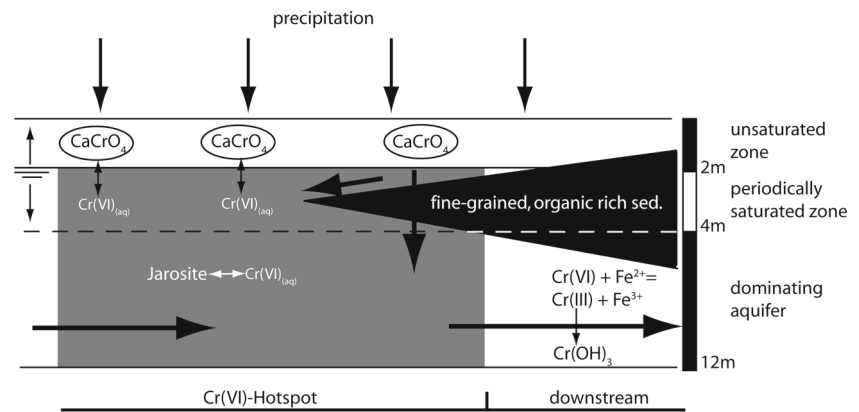
## 2 Benchmark problem setup

### 2.1 Conceptual model

The proposed benchmark problem set is adapted from a series of 2D reactive transport model simulations that were performed to optimize remediation measures for the Cr(VI)-contaminated site located near Rivera (Switzerland) [30]. The focus of these original simulations was on evaluating the extent to which naturally occurring Cr(VI) reduction could be defined as remediation strategy. The simulations were based on an extended field campaign [18] and the subsequently derived conceptual model (Fig. 1, [30]), of which the main points are summarized as follows: The Cr(VI) contamination reaches a depth of up to 10 m and originates from occasional spills of sulfuric ( $\text{H}_2\text{SO}_4$ ) and chromic acid ( $\text{H}_2\text{CrO}_4$ ), occurring during the on-site production of the latter in the 1950s. The interaction between the spilled chromic acid and the Ca-rich concrete of the former processing plant leads to the formation of highly soluble chromate ( $\text{CaCrO}_4$ ). By contrast, the interaction between the chromic and sulfuric acid with the in situ subsurface lead to the precipitation of sparingly soluble Cr(VI) bearing jarosite ( $\text{KFe}_3(\text{SO}_4)_{1.8}(\text{CrO}_4)_{0.2}(\text{OH})_6$ ). Accordingly, current groundwater Cr(VI) concentrations are controlled by the dissolution of these two Cr(VI)-bearing minerals. It was concluded that Cr(VI)-bearing jarosite forms the dominant Cr(VI)-bearing mineral phase within the saturated zone (e.g., dominating aquifer, Fig. 1), whereas infiltrating rainwater and groundwater table variations lead to an additional dissolution of highly soluble chromate ( $\text{CaCrO}_4$ ) accumulated in the unsaturated and periodically saturated zone.

Due to the presence of  $\text{Fe}^{2+}$ -bearing minerals such as annite ( $\text{Fe}^{2+}$ -bearing biotite) and chamosite ( $\text{Fe}^{2+}$ -bearing chlorite) reducing conditions are established and aqueous  $\text{Fe}^{2+}$  is available in excess of Cr(VI). Accordingly, dissolved Cr(VI) is reduced to Cr(III) by a homogenous kinetic reaction with  $\text{Fe}^{2+}$ , introducing Cr isotope fractionation to the system. For the current field site, a minimal Cr(VI) reduction efficiency of 31 % along a 120-m long flow path at a flow velocity of 3.5 m/day was estimated by measuring Cr isotopes and applying a Rayleigh fractionation model [18]. Amorphous  $\text{Cr}(\text{OH})_3$  is assumed to form the ultimate Cr(VI) reduction product because Cr(III) is only sparingly soluble at near neutral pH values [4] such as observed for the Rivera site (pH-range 5.7–6.6). Many studies have shown that the redox change from Cr(VI) to Cr(III) is the

**Fig. 1** Conceptual model of the Rivera site illustrating the major processes that are simulated by the benchmark problem set (adapted from Wanner et al. [30])



strongest contributor to observed Cr isotope fractionation e.g., [12, 20, 42]. Accordingly, no Cr isotope fractionation was assumed during  $\text{Cr}(\text{OH})_3$  precipitation.

In the pH range from 2–6 Cr(VI) concentrations are affected by Cr(VI) sorption to Al- and Fe-hydroxides [43]. In contrast to Cr(VI) reduction, Cr(VI) sorption does not cause significant Cr isotope fractionation [43]. To date, the behavior of Cr(VI) sorption has not been investigated for the Rivera site. Accordingly, the conceptual site model does not include Cr(VI) sorption.

## 2.2 Benchmark problem set

For the benchmark problem set presented here, the monitored natural attenuation (MNA) remediation scenario such as simulated by Wanner et al. [30] is taken as the comprehensive problem. When compared to this original simulation, the benchmark aims to simulate the fate of individual Cr isotopes for various Cr pools (dissolved Cr(VI) and Cr(III), solid Cr(VI) and Cr(III)) and not for dissolved Cr(VI) only.

The benchmark problem is divided into four levels of increasing complexity. The first problem level addresses the simulation of naturally occurring Cr(VI) reduction for a 1D simulation corresponding to an idealized field-scale 1D flow path, along which a Cr(VI) reduction efficiency of 31 % was inferred [18]. The individual isotopes of Cr, kinetic fractionation due to reduction and non-fractionating precipitation are implemented for the 1D domain in problem level #2. The main purpose of level #2 is to ensure that Cr isotope fractionation (aqueous kinetic fractionation and non-fractionating Cr(III) precipitation) is accurately implemented into the different codes. This can be tested using an analytical Rayleigh distillation model because for a 1D homogenous porous media, Cr isotopic fractionation caused by Cr(VI) reduction typically follows such a behavior [15, 17, 21]. Moreover, the comparison between level #1 and level #2 allows testing whether bulk Cr

concentrations remained unchanged when Cr isotope fractionation was added to the simulation.

Level #3 simulates the Cr(VI) plume for a 2D plan view by specifying the site-specific hydrological conditions and the spatial distribution of the Rivera Cr(VI)-contaminated site [18]. It uses the reaction network specified for problem level #1. Level #4 presents the comprehensive problem using the hydrological conditions and spatial distribution of the Cr(VI) contamination specified for problem level #3 with the addition of the Cr isotopic composition of the two Cr(VI) sources and Cr isotope fractionation during aqueous kinetic Cr(VI) reduction. Similar to the two 1D levels, the comparison between level #3 and level #4 allows testing whether the Cr(VI) solubility remains unchanged when the fate of individual Cr isotopes was added to the simulation.

It should be noted that the provided problem set aims to provide a benchmark for simulating fundamental geochemical processes to cause variation in the aqueous Cr isotopic ratio (e.g., kinetic fractionation by aqueous Cr(VI) reduction, non-fractionating Cr(III) precipitation, solubility of various Cr(VI)-bearing minerals). By contrast, we do not provide a benchmark for testing the accurate simulation of transport effects on Cr isotope fractionation (e.g., hydrodynamic dispersion).

## 3 Mathematical model formulations and numerical implementation

The benchmark problem set presented here requires the simulation of isothermal single-phase fluid flow and advective-diffusive transport of dissolved chemical species. The mathematical formulation of these processes and their numerical implementation differ between the different codes used to solve the benchmark. Different numerical implementations include the variable for which it is solved for when simulating fluid flow (e.g., pressure vs. hydraulic heads), the way boundary conditions are formulated (e.g., ghost cells vs.

indefinitely large grid blocks), and the discretization of the model domain (e.g., full vs. half nodes at the model edge). A detailed comparison of the various numerical implementations of fluid flow and transport processes is provided by Steefel et al. [41].

The geochemical reaction network includes aqueous speciation reactions, kinetic mineral reactions, and kinetic aqueous reactions. The corresponding general mathematical formulation for each code is also provided by Steefel et al. [41] and references therein. To fully understand this benchmark, however, the most important equations are summarized below.

### 3.1 Aqueous speciation reactions

Reactions among aqueous species except for the reduction of aqueous Cr(VI) to aqueous Cr(III) (5) are assumed to equilibrate instantaneously. Equilibrium reactions are computed by defining the number of independent chemical components as primary or basis species. Any other species are defined as secondary species. The term secondary is inherited from the fact that these species can be expressed as a linear combination (i.e., chemical reaction) of primary species. Using the law of mass action concentrations of secondary species are thus calculated as a function of the concentration of primary species:

$$c_i = K_i^{-1} \gamma_i^{-1} \prod_{j=1}^{N_C} c_j^{v_{ij}} \gamma_j^{v_{ij}} \quad (1)$$

where  $c_i$  is the molal concentration of the  $i$ th secondary species, and  $c_j$  is the molal concentration of the  $j$ th primary species,  $\gamma_i$  and  $\gamma_j$  refer to thermodynamic activity coefficients of the secondary and primary species, respectively,  $K_i$  is the equilibrium constant, and  $v_{ij}$  refers to the stoichiometric coefficient of  $j$ th basis species in the  $i$ th chemical reaction. Primary species considered in the benchmark are provided in Table 1. Secondary species and their corresponding reaction stoichiometry are listed in Table 2 using positive stoichiometric coefficients ( $v_j$ ) for primary species that are consumed by the listed reactions, and negative  $v_j$  values to denote primary species that are produced. Table 2 also provides corresponding equilibrium constants obtained using SUPCRT92 [44 and references therein] and tabulated in the EQ3/6 database [45] except for thermodynamic Cr data, which were taken from Ball and Nordstrom [46]. Depending on the code, activity coefficients  $\gamma_i$  and  $\gamma_j$  are calculated using various forms of the Debye-Huckel model (see Steefel et al. [41] and references therein for more information). Ion radii ( $r_{e,j}$ ) of primary and secondary species used in conjunction with these Debye-Huckel models are provided in Table 1 and 2.

**Table 1** Primary (component) species and ion radii for Debye-Huckel

Component	Primary species	$r_{e,j}^1$	Charge
c1	H <sup>+</sup>	3.08	1
c2	H <sub>2</sub> O	0	0
c3	Cl <sup>-</sup>	1.81	-1
c4	Na <sup>+</sup>	1.91	1
c5	K <sup>+</sup>	2.27	1
c6	Mg <sup>2+</sup>	2.54	2
c7	Fe <sup>2+</sup>	2.62	2
c8	Fe <sup>3+</sup>	3.46	3
c9	SO <sub>4</sub> <sup>2-</sup>	3.15	-2
c10	CrO <sub>4</sub> <sup>2-</sup>	3	-2
c11	<sup>52</sup> CrO <sub>4</sub> <sup>2-</sup>	3	-2
c12	<sup>53</sup> CrO <sub>4</sub> <sup>2-</sup>	3	-2
c13	NO <sub>3</sub> <sup>-</sup>	2.81	-1
c14	HCO <sub>3</sub> <sup>-</sup>	2.1	-1
c15	Ca <sup>2+</sup>	2.87	2
c16	SiO <sub>2(aq)</sub>	0	0
c17	Cr <sup>3+</sup>	3.6	3
c18	<sup>52</sup> Cr <sup>3+</sup>	3.6	3
c19	<sup>53</sup> Cr <sup>3+</sup>	3.6	3
c20	Al <sup>3+</sup>	3.33	3

<sup>1</sup> $r_{e,j}$  refers to the effective ionic radius that is used in conjunction with various forms of the Debye Hueckel activity model to calculate activity coefficients (see Steefel et al. [41] and references therein for more information)

### 3.2 Mineral dissolution and precipitation reactions

For all of the codes, mineral dissolution and precipitation reaction rates  $r$  (mol kg<sub>H<sub>2</sub>O</sub><sup>-1</sup> s<sup>-1</sup>) are formulated based on transition state theory (TST) [47]

$$r = A \cdot k_{\text{Min}} \exp \left[ \frac{-E_a}{R} \left( \frac{1}{T} - \frac{1}{298.15} \right) \right] \cdot \left[ 1 - \left( \frac{Q}{K} \right)^{m \cdot n} \right] \quad (2)$$

where  $A$  refers to a minerals reactive surface area (m<sub>mineral</sub><sup>2</sup>/kgH<sub>2</sub>O),  $k_{\text{Min}}$  is the reaction rate constant at 25 °C (mol/m<sup>2</sup>/s),  $E_a$  refers to the activation energy (kJ/mol),  $T$  and  $R$  are the temperature (K) and ideal gas constant,  $Q$  refers to the ion activity product of a mineral dissolution/precipitation reaction and  $K$  is the corresponding equilibrium constant. Exponents  $m$  and  $n$  are fitting parameters that must be experimentally determined. For this benchmark they were set to one, which is usually the case, but not always. Equation 2 illustrates that precipitation rates  $r$  are calculated as negative rates (as  $Q/K > 1$ ), whereas dissolution rates are computed as positive rates ( $Q/K < 1$ ). Reaction stoichiometry of mineral reactions considered by any of the benchmark levels are given in Table 3, whereas kinetic

**Table 2** Aqueous complexation reactions and corresponding thermodynamic parameters ( $\log(K), r_{e,j}$ ) used for any of the problem levels

Reaction	Secondary species <sup>1</sup>	$r_{e,j}^2$	Charge	Log(K)	H <sup>+</sup>	H <sub>2</sub> O	Cl <sup>-</sup>	Na <sup>+</sup>	K <sup>+</sup>	Mg <sup>2+</sup>	Fe <sup>2+</sup>	Fe <sup>3+</sup>	SO <sub>4</sub> <sup>2-</sup>	NO <sub>3</sub> <sup>-</sup>	HCO <sub>3</sub> <sup>-</sup>	Ca <sup>2+</sup>	SiO <sub>2(aq)</sub>	Al <sup>3+</sup>	
				(25°)															
a1	NaOH <sub>(aq)</sub>	3	0	14.799	-1	1	0	1	0	0	0	0	0	0	0	0	0	0	
a2	AlO <sub>2</sub> <sup>-</sup>	1.81	-1	22.199	-4	2	0	0	0	0	0	0	0	0	0	0	0	1	
a3	AlO <sup>+</sup>	2.31	1	10.343	-2	1	0	0	0	0	0	0	0	0	0	0	0	1	
a4	AlOH <sup>2+</sup>	2.8	2	5	-1	1	0	0	0	0	0	0	0	0	0	0	0	1	
a5	HAIO <sub>2(aq)</sub>	0	0	15.604	-3	2	0	0	0	0	0	0	0	0	0	0	0	1	
a6	CO <sub>2(aq)</sub>	0	0	-6.341	1	-1	0	0	0	0	0	0	0	1	0	0	0	0	
a7	CO <sub>3</sub> <sup>2-</sup>	2.81	-2	10.325	-1	0	0	0	0	0	0	0	0	1	0	0	0	0	
a8	CaCO <sub>3(aq)</sub>	0	0	7.009	-1	0	0	0	0	0	0	0	0	1	1	0	0	0	
a9	CaHCO <sub>3</sub>	2.31	1	-1.043	0	0	0	0	0	0	0	0	0	1	1	0	0	0	
a10	CaOH <sup>+</sup>	2.31	1	12.834	-1	1	0	0	0	0	0	0	0	0	1	0	0	0	
a11	CaSO <sub>4(aq)</sub>	0	0	-2.1	0	0	0	0	0	0	0	1	0	0	1	0	0	0	
a12	HFeO <sub>2</sub> <sup>-</sup>	1.81	-1	29.202	-3	2	0	0	0	0	1	0	0	0	0	0	0	0	
a13	FeCl <sup>-</sup>	2.31	1	0.165	0	0	1	0	0	0	1	0	0	0	0	0	0	0	
a14	FeO <sup>+</sup>	2.31	1	5.652	-2	1	0	0	0	0	0	1	0	0	0	0	0	0	
a15	FeCl <sub>2(aq)</sub>	0	0	8.181	0	0	2	0	0	0	1	0	0	0	0	0	0	0	
a16	FeO <sub>(aq)</sub>	0	0	20.412	-2	1	0	0	0	0	1	0	0	0	0	0	0	0	
a17	FeOH <sup>+</sup>	2.31	1	9.315	-1	1	0	0	0	0	1	0	0	0	0	0	0	0	
a18	FeO <sub>2</sub> <sup>-</sup>	1.81	-1	21.618	-4	2	0	0	0	0	0	1	0	0	0	0	0	0	
a19	FeOH <sup>2+</sup>	2.8	2	2.205	-1	1	0	0	0	0	0	1	0	0	0	0	0	0	
a20	FeSO <sub>4(aq)</sub>	0	0	-2.2	0	0	0	0	0	0	1	0	1	0	0	0	0	0	
a21	FeSO <sub>4</sub> <sup>+</sup>	2.31	1	-1.917	0	0	0	0	0	0	0	1	1	0	0	0	0	0	
a22	HFeO <sub>2(aq)</sub>	0	0	12.021	-3	2	0	0	0	0	0	1	0	0	0	0	0	0	
a23	FeCl <sup>2+</sup>	2.8	2	-1.475	0	0	1	0	0	0	0	1	0	0	0	0	0	0	
a24	HNO <sub>3(aq)</sub>	0	0	1.308	1	0	0	0	0	0	0	0	0	1	0	0	0	0	
a25	H <sub>2</sub> SO <sub>4(aq)</sub>	0	0	1.021	2	0	0	0	0	0	0	0	1	0	0	0	0	0	
a26	HSO <sub>4</sub> <sup>-</sup>	2.37	-1	-1.975	1	0	0	0	0	0	0	0	1	0	0	0	0	0	
a27	HSiO <sub>3</sub> <sup>-</sup>	1.81	-1	9.836	-1	1	0	0	0	0	0	0	0	0	0	0	1	0	
a28	KHSO <sub>4(aq)</sub>	0	0	1.502	1	0	0	0	1	0	0	0	1	0	0	0	0	0	
a29	KSO <sub>4</sub> <sup>-</sup>	1.81	-1	-0.875	0	0	0	0	1	0	0	0	1	0	0	0	0	0	
a30	MgCO <sub>3(aq)</sub>	0	0	7.356	-1	0	0	0	0	1	0	0	0	0	1	0	0	0	
a31	MgHCO <sub>3</sub> <sup>+</sup>	2.31	1	-1.033	0	0	0	0	0	1	0	0	0	0	1	0	0	0	
a32	MgOH <sup>+</sup>	2.31	1	11.682	-1	1	0	0	0	1	0	0	0	0	0	0	0	0	
a33	MgSO <sub>4(aq)</sub>	0	0	-2.22	0	0	0	0	0	1	0	0	1	0	0	0	0	0	
a34	NaHCO <sub>3(aq)</sub>	0	0	-0.149	0	0	0	1	0	0	0	0	0	0	1	0	0	0	
a35	NaSO <sub>4</sub> <sup>-</sup>	1.81	-1	-0.696	0	0	0	1	0	0	0	0	1	0	0	0	0	0	
a36	OH <sup>-</sup>	1.4	-1	13.991	-1	1	0	0	0	0	0	0	0	0	0	0	0	0	

<sup>1</sup>No Cr complexes were considered

<sup>2</sup> $r_{e,j}$  refers to the effective ionic radius that is used in conjunction with various forms of the Debye Hueckel activity model to calculate activity coefficients (see Steefel et al. [41] and references therein for more information)

and thermodynamic parameters are provided in Table 4. The model temperature was set to 25 °C. Consequently, the effective rate constant is equal to the one at 25 °C ( $k_{Min}$ , Table 4) and activation energies are irrelevant to calculate reaction rates.

### 3.2.1 Reactive surface area of primary minerals

For initially present (i.e., primary) minerals, reactive surface areas provided in Table 4 refer to bulk reactive surface areas  $A_m$  ( $m^2_{mineral}/m^3_{medium}$ ). They are converted into units

**Table 3** Mineral reactions used for any of the problem levels

Reaction	Minerals	H <sup>+</sup>	H <sub>2</sub> O	Cl <sup>-</sup>	Na <sup>+</sup>	K <sup>+</sup>	Mg <sup>2+</sup>	Fe <sup>2+</sup>	Fe <sup>3+</sup>	SO <sub>4</sub> <sup>2-</sup>	CrO <sub>4</sub> <sup>2-</sup>	<sup>52</sup> CrO <sub>4</sub> <sup>2-</sup>	<sup>53</sup> CrO <sub>4</sub> <sup>2-</sup>	NO <sub>3</sub> <sup>-</sup>	HCO <sub>3</sub> <sup>-</sup>	Ca <sup>2+</sup>	SiO <sub>2(aq)</sub>	Cr <sup>3+</sup>	<sup>52</sup> Cr <sup>3+</sup>	<sup>53</sup> Cr <sup>3+</sup>	Al <sup>3+</sup>	
m1	Cr(OH) <sub>3(am)</sub>	-3	3	0	0	0	0	0	0	0	0	0	0	0	0	0	0	1	0	0	0	0
m2	CO <sub>2(s)</sub>	1	-1	0	0	0	0	0	0	0	0	0	0	0	1	0	0	0	0	0	0	0
m3	Cr-Jarosite <sup>1</sup>	-6	6	0	0	1	0	0	3	1.8	0.2	0	0	0	0	0	0	0	0	0	0	0
m4	CaCrO <sub>4(s)</sub> <sup>1</sup>	0	0	0	0	0	0	0	0	0	1	0	0	0	0	1	0	0	0	0	0	0
m5	CaCrO <sub>4(s)</sub> -Iso <sup>1</sup>	0	0	0	0	0	0	0	0	0	0	0.898156	0.101844	0	0	1	0	0	0	0	0	0
m6	Cr-Jarosite-Iso <sup>1</sup>	-6	6	0	0	1	0	0	3	1.8	0	0.179631	0.020369	0	0	0	0	0	0	0	0	0
m7	<sup>52</sup> Cr(OH) <sub>3(am)</sub> <sup>2</sup>	-3	3	0	0	0	0	0	0	0	0	0	0	0	0	0	0	0	0	1	0	0
m8	<sup>53</sup> Cr(OH) <sub>3(am)</sub> <sup>2</sup>	-3	3	0	0	0	0	0	0	0	0	0	0	0	0	0	0	0	0	0	1	0
m9	Chamosite	-10	7	0	0	0	0	2	0	0	0	0	0	0	0	0	1	0	0	0	0	2
m10	Quartz	0	0	0	0	0	0	0	0	0	0	0	0	0	0	0	1	0	0	0	0	0
m11	Annite	-10	6	0	0	0	1	0	3	0	0	0	0	0	0	0	3	0	0	0	0	1

<sup>1</sup>Dissolution only

<sup>2</sup>Specified as solid solution

of  $m_{\text{mineral}}^2/\text{kg}_{\text{H}_2\text{O}}$  to calculate the effective reactive surface area  $A$  that goes into the reaction rate (2)

$$A = \frac{A_m}{\rho_w \cdot \varphi} \tag{3}$$

where  $\rho_w$  is the water density (997.16  $\text{kg}_{\text{H}_2\text{O}}/\text{m}^3_{\text{water}}$  at 25 °C),  $\varphi$  is the porosity of the porous medium ( $\text{m}^3_{\text{water}}/\text{m}^3_{\text{medium}}$ ) and  $A_m$  refer to the reactive surface areas provided in Table 4 ( $\text{m}^2_{\text{mineral}}/\text{m}^3_{\text{medium}}$ ).

### 3.2.2 Reactive surface area of secondary minerals

The calculation of reactive surface areas of newly formed (i.e., secondary) minerals (e.g.,  $\text{Cr}(\text{OH})_3$ ) differs between the different codes used so solve this benchmark.

TOUGHREACT and CRUNCHLOW are using specific reactive surface areas to calculate reactive surface areas ( $A_{2\text{nd}}, m_{\text{mineral}}^2/\text{kg}_{\text{H}_2\text{O}}$ ) used in conjunction with Eq. 2

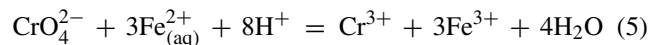
$$A_{2\text{nd}} = \frac{V_{\text{frac}} \cdot A_{\text{specific}}}{\rho_w \cdot \varphi} \tag{4}$$

where  $V_{\text{frac}}$  refers to the mineral volume fraction ( $\text{m}^3_{\text{mineral}}/\text{m}^3_{\text{medium}}$ ), and  $A_{\text{specific}}$  is the corresponding specific surface area ( $\text{m}^2_{\text{mineral}}/\text{m}^3_{\text{mineral}}$ ). By doing so, a minimum threshold volume fraction ( $V_{\text{frac}}$ ) has to be defined to calculate the surface area ( $A_{2\text{nd}}$ ) of the very first mineral amount that precipitates (Table 4).

In simulations carried out by MIN3P and FLOTRAN, constant reactive surface areas were used for newly formed secondary minerals (Table 4). In case of MIN3P, minimum initial volume fractions  $V_{\text{frac}}^0 > 0$  have to be specified. It should be noted that these minimum volume fractions refer to true volume fractions, whereas TOUGHREACT and CRUNCHFLOW are only using minimum volume fractions to calculate  $A_{2\text{nd}}$  (4) and zero mineral volume fractions can be handled.

### 3.3 Kinetic aqueous reactions

Cr(VI) reduction is modeled as an aqueous kinetic reaction using aqueous Fe(II) as the reductant:



Generally, kinetic Cr(VI) reduction by aqueous Fe(II) (5) follows a first-order reaction rate with respect to aqueous Fe(II) as well as Cr(VI) [48]. At the Rivera site, however, Fe(II) is available mostly in excess of Cr(VI) [18]. Accordingly, for this benchmark the reaction rate  $r$  ( $\text{mol}_{\text{kg}_{\text{H}_2\text{O}}}^{-1}\text{s}^{-1}$ ) for Eq. 5 is specified as a first-order reaction rate solely with respect to the total Cr(VI) concentration and no dependence on total Fe(II) concentration was considered

$$r = k \cdot (\text{CrO}_4^{2-})_{\text{Total}} \tag{6}$$

**Table 4** Thermodynamic and kinetic parameters of mineral reactions used for any of the problem levels

Minerals	Formula	Molar volume (cm <sup>3</sup> /mol)	Log(K)(25°C) <sup>5</sup>	Log(k <sub>Min</sub> ) (mol kg <sub>H2O</sub> <sup>-1</sup> m <sup>-2</sup> s <sup>-1</sup> ) <sup>5</sup>	A <sub>m</sub> (m <sup>2</sup> <sub>mineral</sub> /m <sup>3</sup> <sub>medium</sub> ) <sup>2</sup>	
m1	Cr(OH) <sub>3(am)</sub>	Cr(OH) <sub>3</sub>	29.09	9.35	-4	1 <sup>3</sup>
m2	CO <sub>2(s)</sub>	CO <sub>2</sub>	1.00	-9.5	-4	1
m3	Cr-Jarosite	KFe <sub>3</sub> (SO <sub>4</sub> ) <sub>1.8</sub> (CrO <sub>4</sub> ) <sub>0.2</sub> (OH) <sub>6</sub>	100.44	-12	-5	1
m4	CaCrO <sub>4(s)</sub>	CaCrO <sub>4</sub>	98.32	-8.6	-3	1
m5	CaCrO <sub>4(s)</sub> – Iso	Ca <sup>52</sup> Cr <sub>0.89816</sub> <sup>53</sup> Cr <sub>0.10184</sub> O <sub>4</sub>	98.32	-8.742933 <sup>4</sup>	-3	1
m6	Cr-Jarosite-Iso	KFe <sub>3</sub> (SO <sub>4</sub> ) <sub>1.8</sub> ( <sup>52</sup> Cr <sub>0.89816</sub> <sup>53</sup> Cr <sub>0.10184</sub> O <sub>4</sub> ) <sub>0.2</sub> (OH) <sub>6</sub>	100.44	-12.0285866 <sup>4</sup>	-5	1
m7	<sup>52</sup> Cr(OH) <sub>3(am)</sub> <sup>1</sup>	<sup>52</sup> Cr(OH) <sub>3</sub>	29.09	9.350	-8	1 <sup>3</sup>
m8	<sup>53</sup> Cr(OH) <sub>3(am)</sub> <sup>1</sup>	<sup>53</sup> Cr(OH) <sub>3</sub>	29.09	9.350	-8	1 <sup>3</sup>
m9	Chamosite	Fe <sub>2</sub> Al <sub>2</sub> SiO <sub>5</sub> (OH) <sub>4</sub>	106.20	32.837	-12	1
m10	Quartz	SiO <sub>2</sub>	22.69	-3.752	-13.4	1
m11	Annite	KFe <sub>3</sub> AlSi <sub>3</sub> O <sub>10</sub> (OH) <sub>2</sub>	154.32	29.453	-9.5	1

<sup>1</sup>Specified as solid solution

<sup>2</sup>Specified values refer to bulk surface areas except for m1, m7 and m8 (see note below)

<sup>3</sup>Values refer to constant reactive surface areas used by MIN3P, and FLOTTRAN to calculate the precipitation rate of these newly formed phases. Using TOUGHREACT and CRUNCHFLOW, specific surface areas of 1 m<sup>2</sup><sub>mineral</sub>/g<sub>mineral</sub> were used in conjunction with Eq. 4 to calculate evolving reactive surface area. For these codes, initial volume fractions of 1e-10, 8.981529e-11 and 1.018437e-11 were specified to calculate the surface area of the very first amount of precipitated Cr(OH)<sub>3</sub> (m1), <sup>52</sup>Cr(OH)<sub>3</sub> (m7), and <sup>53</sup>Cr(OH)<sub>3</sub> (m8)

<sup>4</sup>Log(K) values do not have to be adjusted using MIN3P and the values specified for (m3) and (m4) can be used to simulate problem level #4

<sup>5</sup>Specified according to Wanner et al. [30]

where  $k$  (s<sup>-1</sup>) is the reaction rate constant and  $(CrO_4^{2-})_{Total}$  refers to the total Cr(VI) concentration. To obtain the observed 31 % Cr(VI) reduction along a 120-m flow path at an average linear flow velocity of 3.5 m/day [18],  $k$  was set to  $1.268 \times 10^{-7} s^{-1}$ .

### 3.4 Simulating the fate of individual Cr isotopes

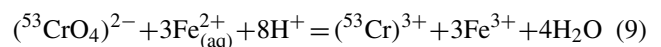
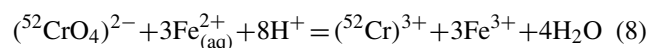
Cr isotope composition is typically expressed as a  $\delta$  value given in per mil

$$\delta^{53}Cr_{SRM979} = \frac{R(^{53}Cr/^{52}Cr)_{modeled}}{R(^{53}Cr/^{52}Cr)_{SRM979}} - 1 \quad (7)$$

where  $R(^{53}Cr/^{52}Cr)_{modeled}$  and  $R(^{53}Cr/^{52}Cr)_{SRM979}$  refer to the simulated <sup>53</sup>Cr/<sup>52</sup>Cr ratio as well as to the corresponding ratio of the certified standard SRM979 [49], which is 0.11339. Equation 7 and any other expression related to simulated stable Cr isotope ratios is following the guidelines recently presented by Coplen [50].

#### 3.4.1 Cr isotope fractionation during kinetic aqueous Cr(VI) reduction

For the problem levels simulating Cr isotope fractionation (#2, #4), we make the simplification (i.e., assumption) that <sup>52</sup>Cr and <sup>53</sup>Cr sum up to 100 % bulk Cr (<sup>52</sup>Cr + <sup>53</sup>Cr = Cr<sub>Total</sub>) even though they only represent about 93 % of total Cr [49]. Accordingly, we do not simulate the fate of the two minor Cr isotopes (<sup>50</sup>Cr and <sup>54</sup>Cr). The fate of <sup>52</sup>Cr and <sup>53</sup>Cr during Cr(VI) reduction is simulated by replacing Eq. 5 by two separate equations for the two major isotopologues of aqueous Cr(VI) (<sup>52</sup>CrO<sub>4</sub>)<sup>2-</sup> and (<sup>53</sup>CrO<sub>4</sub>)<sup>2-</sup>:



As modeled here, kinetic Cr isotope fractionation is caused by different reduction rates for (<sup>52</sup>CrO<sub>4</sub>)<sup>2-</sup> (<sup>52</sup>r) and (<sup>53</sup>CrO<sub>4</sub>)<sup>2-</sup> (<sup>53</sup>r). This distinction was implemented in each of the codes utilized for this benchmark. TOUGHREACT

[51], FLOTRAN [52], and CRUNCHFLOW [53 and references therein] employed the method described for C isotope fractionation [36]. In doing so, the concentrations of the specific Cr(VI) isotopologues were used to calculate  $^{52}r$  and  $^{53}r$

$$^{52}r = k \cdot \left( ^{52}\text{CrO}_4 \right)_{\text{Total}}^{2-} \quad (10)$$

$$^{53}r = k \cdot \left( ^{53}\text{CrO}_4 \right)_{\text{Total}}^{2-} \cdot \alpha^{53}\text{Cr}_{\text{Cr(III)/Cr(VI)}} \quad (11)$$

where  $k$  ( $\text{s}^{-1}$ ) corresponds to the reaction rate constant used for the reduction of bulk Cr(VI) ((6);  $1.268 \times 10^{-7} \text{ s}^{-1}$ ), and  $\left( ^{52}\text{CrO}_4 \right)_{\text{Total}}^{2-}$  and  $\left( ^{53}\text{CrO}_4 \right)_{\text{Total}}^{2-}$  refer to the total concentrations of  $\left( ^{52}\text{CrO}_4 \right)^{2-}$  and  $\left( ^{53}\text{CrO}_4 \right)^{2-}$ . The term  $\alpha^{53}\text{Cr}_{\text{Cr(III)/Cr(VI)}}$  denotes the Cr isotopic fractionation factor, which defines the magnitude of Cr isotope fractionation based on the ratio of the instantaneous  $^{53}\text{Cr}/^{52}\text{Cr}$  ratio of the product  $R(^{53}\text{Cr}/^{52}\text{Cr})_{\text{Cr(III)}}$  to the residual reactant  $R(^{53}\text{Cr}/^{52}\text{Cr})_{\text{Cr(VI)}}$ :

$$\alpha^{53}\text{Cr}_{\text{Cr(III)/Cr(VI)}} = \frac{R(^{53}\text{Cr}/^{52}\text{Cr})_{\text{Cr(III)}}}{R(^{53}\text{Cr}/^{52}\text{Cr})_{\text{Cr(VI)}}} \quad (12)$$

Cr(VI) reduction experiments with soil samples having a similar mineralogical composition to the Rivera aquifer were performed by Ellis et al. [20] yielding a fractionation factor of 0.9966. Accordingly,  $\alpha^{53}\text{Cr}_{\text{Cr(III)/Cr(VI)}}$  was set to 0.9966 for the problem set presented here.

In contrast to the other codes, MIN3P [29, 34, 54] computes  $^{52}r$  and  $^{53}r$  by using the total Cr(VI) concentration and specific reaction rate constants for  $\left( ^{52}\text{CrO}_4 \right)^{2-}$  ( $^{52}k$ ) and  $\left( ^{53}\text{CrO}_4 \right)^{2-}$  ( $^{53}k$ ) assuming that  $^{52}k$  and  $^{53}k$  sum up to the reaction rate constant of bulk Cr(VI)  $k$  (6):

$$\begin{aligned} ^{52}r &= ^{52}k \cdot \left( \text{CrO}_4^{2-} \right)_{\text{Total}} \\ &= \frac{k}{1 + \alpha^{53}\text{Cr}_{\text{Cr(III)/Cr(VI)}} \cdot R(^{53}\text{Cr}/^{52}\text{Cr})_{\text{Cr(VI)}}} \\ &\quad \times \left( \text{CrO}_4^{2-} \right)_{\text{Total}} \end{aligned} \quad (13)$$

$$\begin{aligned} ^{53}r &= ^{53}k \cdot \left( \text{CrO}_4^{2-} \right)_{\text{Total}} \\ &= \frac{k \cdot \alpha^{53}\text{Cr}_{\text{Cr(III)/Cr(VI)}} \cdot R(^{53}\text{Cr}/^{52}\text{Cr})_{\text{Cr(VI)}}}{1 + \alpha^{53}\text{Cr}_{\text{Cr(III)/Cr(VI)}} \cdot R(^{53}\text{Cr}/^{52}\text{Cr})_{\text{Cr(VI)}}} \\ &\quad \times \left( \text{CrO}_4^{2-} \right)_{\text{Total}} \end{aligned} \quad (14)$$

For any approach,  $^{52}r$  and  $^{53}r$  sum up to an overall reaction rate that is very close to the one used for problem level #1 (6) ensuring that the overall Cr(VI) reduction rate was essentially the same for levels #1 and #2 as well as for #3 and #4

$$\begin{aligned} \left( ^{52}r + ^{53}r \right)_1 &= k \cdot \left[ \left( ^{52}\text{CrO}_4 \right)^{2-} + \left( ^{53}\text{CrO}_4 \right)^{2-} \cdot \alpha^{53}\text{Cr}_{\text{Cr(III)/Cr(VI)}} \right] \\ &\quad (15) \end{aligned}$$

$$\left( ^{52}r + ^{53}r \right)_2 = k \cdot \left[ \left( ^{52}\text{CrO}_4 \right)^{2-} + \left( ^{53}\text{CrO}_4 \right)^{2-} \right] \quad (16)$$

where  $\left( ^{52}r + ^{53}r \right)_1$  refers to the sum of  $^{52}r$  and  $^{53}r$  of the TOUGHREACT, CRUNCHFLOW, and FLOTRAN approach, whereas  $\left( ^{52}r + ^{53}r \right)_2$  refers to the corresponding MIN3P approach. Equation 15 implies that the overall Cr(VI) reduction rate for the TOUGHREACT, CRUNCHFLOW, and FLOTRAN approach is slightly smaller than the one for the bulk problems (levels #1 and #3). However, the rate difference is less than 0.1 % because the normalized bulk earth fraction of  $^{53}\text{Cr}$  is on the order of 10 % and  $\alpha^{53}\text{Cr}_{\text{Cr(III)/Cr(VI)}}$  was set to 0.9966, which justifies the chosen approach.

### 3.4.2 Nonfractionating precipitation of $\text{Cr}(\text{OH})_3$

In all of the codes,  $\left( ^{52}\text{Cr} \right)^{3+}$  and  $\left( ^{53}\text{Cr} \right)^{3+}$  precipitate as an ideal  $^{52}\text{Cr}(\text{OH})_3$ – $^{53}\text{Cr}(\text{OH})_3$  solid solution to remove both Cr(III) isotopologues produced by reactions 8 and 9. To do so,  $^{52}\text{Cr}(\text{OH})_3$  and  $^{53}\text{Cr}(\text{OH})_3$  are defined as end-members (reactions m7 and m8, Table 3). “Ideal” means that for a given composition, the activities of the two end-members,  $a_{x\text{Cr}(\text{OH})_3}$ , are equal to the corresponding mole fractions,  $x_{x\text{Cr}(\text{OH})_3}$ , in the solid solution (i.e., activity coefficient = 1). The overall precipitation rate of the  $^{52}\text{Cr}(\text{OH})_3$ – $^{53}\text{Cr}(\text{OH})_3$  solid solution,  $^{ss}r$ , is the sum of the precipitation rate of the two end-members

$$^{ss}r = ^{52}\text{Cr}(\text{OH})_3r + ^{53}\text{Cr}(\text{OH})_3r \quad (17)$$

where  $^{52}\text{Cr}(\text{OH})_3r$  and  $^{53}\text{Cr}(\text{OH})_3r$  refer to the precipitation rate of the two end-members ( $\text{mol kg}_{\text{H}_2\text{O}}^{-1} \text{ s}^{-1}$ ). The calculation of  $^{52}\text{Cr}(\text{OH})_3r$  and  $^{53}\text{Cr}(\text{OH})_3r$  differs between the different codes used to solve this benchmark. The corresponding numerical implementation is described as follows illustrating that for any code, the precipitation of Cr(III) does not cause Cr isotope fractionation.

*TOUGHREACT and FLOTRAN* Using TOUGHREACT [21] and FLOTRAN [52], the precipitation rate for the

$^{52}\text{Cr}(\text{OH})_3$  and  $^{53}\text{Cr}(\text{OH})_3$  end-members is calculated according to

$$^{52}\text{Cr}(\text{OH})_3 r = A_{\text{ss}} \cdot k_{\text{Min}} \cdot \left(1 - \frac{Q_{^{52}\text{Cr}(\text{OH})_3}}{K_{^{52}\text{Cr}(\text{OH})_3}}\right) + k_{\text{Min}} \cdot A_{\text{ss}} \cdot (x_{^{52}\text{Cr}(\text{OH})_3} - 1) \tag{18}$$

$$^{53}\text{Cr}(\text{OH})_3 r = A_{\text{ss}} \cdot k_{\text{Min}} \cdot \left(1 - \frac{Q_{^{53}\text{Cr}(\text{OH})_3}}{K_{^{53}\text{Cr}(\text{OH})_3}}\right) + k_{\text{Min}} \cdot A_{\text{ss}} \cdot (x_{^{53}\text{Cr}(\text{OH})_3} - 1) \tag{19}$$

where  $A_{\text{ss}}$  ( $\text{m}^2_{\text{mineral}}/\text{kgH}_2\text{O}$ ) refers to the reactive surface area of the solid solution (Table 4),  $k_{\text{min}}$  is the reaction rate constant of the solid solution ( $\text{molkg}^{-1}_{\text{H}_2\text{O}} \text{m}^{-2}\text{s}^{-1}$ , Table 4),  $Q_{^{52}\text{Cr}(\text{OH})_3}$  and  $Q_{^{53}\text{Cr}(\text{OH})_3}$  refer to the ion activity product of reactions m7 and m8 (Table 3),  $K_{^{52}\text{Cr}(\text{OH})_3}$  and  $K_{^{53}\text{Cr}(\text{OH})_3}$  are the corresponding equilibrium constants, and  $x_{^{52}\text{Cr}(\text{OH})_3}$  and  $x_{^{53}\text{Cr}(\text{OH})_3}$  are the mole fractions of the precipitating end-members. The first term of Eqs. 18 and 19 refers to the precipitation rate of the corresponding end-member as pure minerals (i.e., maximum rate). The second term ensures that end-members precipitation rates linearly decrease with decreasing mole fraction (as  $x_{\text{Cr}(\text{OH})_3} - 1 < 0$ ). To ensure that the volume ratio of these end-members reflect the fluid composition,  $x_{^{52}\text{Cr}(\text{OH})_3}$  and  $x_{^{53}\text{Cr}(\text{OH})_3}$  are calculated according to

$$x_{^{52}\text{Cr}(\text{OH})_3} = \frac{Q_{^{52}\text{Cr}(\text{OH})_3}/K_{^{52}\text{Cr}(\text{OH})_3}}{Q_{^{52}\text{Cr}(\text{OH})_3}/K_{^{52}\text{Cr}(\text{OH})_3} + Q_{^{53}\text{Cr}(\text{OH})_3}/K_{^{53}\text{Cr}(\text{OH})_3}} \tag{20}$$

$$x_{^{53}\text{Cr}(\text{OH})_3} = \frac{Q_{^{53}\text{Cr}(\text{OH})_3}/K_{^{53}\text{Cr}(\text{OH})_3}}{Q_{^{52}\text{Cr}(\text{OH})_3}/K_{^{52}\text{Cr}(\text{OH})_3} + Q_{^{53}\text{Cr}(\text{OH})_3}/K_{^{53}\text{Cr}(\text{OH})_3}} \tag{21}$$

where  $(Q_{^{52}\text{Cr}(\text{OH})_3}/K_{^{52}\text{Cr}(\text{OH})_3})$  and  $(Q_{^{53}\text{Cr}(\text{OH})_3}/K_{^{53}\text{Cr}(\text{OH})_3})$  refer to the  $Q/K$  ratio of reactions m7 and m8, respectively (Table 3).

By setting  $K_{^{52}\text{Cr}(\text{OH})_3} = K_{^{53}\text{Cr}(\text{OH})_3}$  as well as by using a constant reactive surface area and reaction rate constant ( $A_{\text{ss}}$  and  $k_{\text{Min}}$ ) (Table 4), the ratio of the two precipitation rates,  $(^{53}\text{Cr}(\text{OH})_3 r / ^{52}\text{Cr}(\text{OH})_3 r)$  reflects the aqueous  $(^{53}\text{Cr})^{3+} / (^{52}\text{Cr})^{3+}$  ratio  $(R(^{53}\text{Cr}/^{52}\text{Cr})_{\text{Cr(III)}})$  and no Cr isotope fractionation is introduced by the precipitation of the  $^{52}\text{Cr}(\text{OH})_3 - ^{53}\text{Cr}(\text{OH})_3$  solid solution.

**CRUNCHFLOW** Using CRUNCHFLOW [25],  $^{52}\text{Cr}(\text{OH})_3$  and  $^{53}\text{Cr}(\text{OH})_3$  precipitation rates are calculated according to

$$^{52}\text{Cr}(\text{OH})_3 r = A_{\text{ss}} \cdot k_{\text{min}} \cdot x_{^{52}\text{Cr}(\text{OH})_3} \times \left(1 - \frac{Q_{^{52}\text{Cr}(\text{OH})_3}}{K_{\text{ss}} \cdot x_{^{52}\text{Cr}(\text{OH})_3}}\right) \tag{22}$$

$$^{53}\text{Cr}(\text{OH})_3 r = A_{\text{ss}} \cdot k_{\text{min}} \cdot x_{^{53}\text{Cr}(\text{OH})_3} \times \left(1 - \frac{Q_{^{53}\text{Cr}(\text{OH})_3}}{K_{\text{ss}} \cdot x_{^{53}\text{Cr}(\text{OH})_3}}\right) \tag{23}$$

with  $x_{^{52}\text{Cr}(\text{OH})_3}$  and  $x_{^{53}\text{Cr}(\text{OH})_3}$  calculated according to

$$x_{^{52}\text{Cr}(\text{OH})_3} = \frac{(^{52}\text{Cr})^{3+}}{\text{Cr}_{\text{Total}}^{3+}} \tag{24}$$

$$x_{^{53}\text{Cr}(\text{OH})_3} = \frac{(^{53}\text{Cr})^{3+}}{\text{Cr}_{\text{Total}}^{3+}} \tag{25}$$

By analogy of the TOUGHREACT and FLOTTRAN approach, the absence of fractionation during Cr(III) precipitation was ensured by setting  $K_{^{52}\text{Cr}(\text{OH})_3} = K_{^{53}\text{Cr}(\text{OH})_3}$  as well as by using a constant reactive surface area and reaction rate constant ( $A_{\text{ss}}$  and  $k_{\text{Min}}$ ) (Table 4). It should be noted that for the precipitation of the specified  $^{52}\text{Cr}(\text{OH})_3 - ^{53}\text{Cr}(\text{OH})_3$  solid solution the TOUGHREACT/FLOTTRAN calculation (18–21) is fully equivalent to the one used by CRUNCHFLOW (22–25). For solid solutions with more than two end-members, the different implementation may cause different results, which was however not tested by this benchmark.

**MIN3P** Using MIN3P,  $^{52}\text{Cr}(\text{OH})_3$  and  $^{53}\text{Cr}(\text{OH})_3$  precipitation rates are calculated according to

$$^{52}\text{Cr}(\text{OH})_3 r = A_{\text{ss}} \cdot ^{52}k \cdot \left(1 - \frac{Q_{\text{Cr}(\text{OH})_3}}{K_{\text{Cr}(\text{OH})_3}}\right) \tag{26}$$

$$^{53}\text{Cr}(\text{OH})_3 r = A_{\text{ss}} \cdot ^{53}k \cdot \left(1 - \frac{Q_{\text{Cr}(\text{OH})_3}}{K_{\text{Cr}(\text{OH})_3}}\right) \tag{27}$$

with end-member specific reaction rate constants,  $^{52}k$  and  $^{53}k$ , defined as

$$^{52}k = \frac{k_{\text{Bulk}}}{1 + R(^{53}\text{Cr}/^{52}\text{Cr})_{\text{Cr(III)}}} \tag{28}$$

$$^{53}k = \frac{k_{\text{Bulk}} \cdot R(^{53}\text{Cr}/^{52}\text{Cr})_{\text{Cr(III)}}}{1 + R(^{53}\text{Cr}/^{52}\text{Cr})_{\text{Cr(III)}}} \tag{29}$$

where  $R(^{53}\text{Cr}/^{52}\text{Cr})_{\text{Cr(III)}}$  refers to the ratio between the total dissolved  $(^{53}\text{Cr})^{3+}$  and total dissolved  $(^{52}\text{Cr})^{3+}$  concentration, and  $k_{\text{Bulk}}$  is the reaction rate constant of bulk  $\text{Cr}(\text{OH})_3$  (reaction m1). Combining Eqs. 28 and 29 yields  $^{53}k/^{52}k = R(^{53}\text{Cr}/^{52}\text{Cr})_{\text{Cr(III)}}$ , thus illustrating that the ratio of the two precipitation rates,  $(^{53}\text{Cr}(\text{OH})_3)_r/^{52}\text{Cr}(\text{OH})_3)_r$ , reflects  $R(^{53}\text{Cr}/^{52}\text{Cr})_{\text{Cr(III)}}$  as well. Accordingly, by setting  $K_{^{52}\text{Cr}(\text{OH})_3} = K_{^{53}\text{Cr}(\text{OH})_3}$ , no Cr isotope fractionation is introduced by Cr(III) precipitation.

### 3.4.3 Solubility of Cr bearing minerals

**Jarosite and chromatite** For the two 2D problem levels (#3, #4), aqueous Cr(VI) is inherited from the dissolution of Cr(VI)-bearing jarosite and chromatite. To add the fate of individual Cr isotopes to the 2D problem (level #4) bulk Cr is replaced by  $^{52}\text{Cr}$  and  $^{53}\text{Cr}$  (i.e.,  $\text{Cr}_{\text{Total}} = ^{52}\text{Cr} + ^{53}\text{Cr}$ ) in the corresponding reaction stoichiometry (Table 4). As a consequence, the expression for the equilibrium constant of the two minerals slightly differs depending on whether the fate of the individual Cr isotopes is considered or not. For instance, the equilibrium constants for bulk chromatite ( $K_{\text{CaCrO}_4}$ ) and  $^{52}\text{Cr}$ - and  $^{53}\text{Cr}$ -bearing chromatite ( $K_{\text{CaCrO}_4\text{-Iso}}$ ) are expressed as

$$K_{\text{CaCrO}_4} = \frac{a_{\text{Ca}^{2+}} \cdot a_{\text{CrO}_4^{2-}}}{a_{\text{CaCrO}_4(\text{s})}} \quad (30)$$

$$\begin{aligned} K_{\text{CaCrO}_4\text{-Iso}} &= \frac{a_{\text{Ca}^{2+}} \cdot (a_{^{52}\text{CrO}_4^{2-}})^{\nu_{^{52}\text{Cr}}} \cdot (a_{^{53}\text{CrO}_4^{2-}})^{\nu_{^{53}\text{Cr}}}}{a_{\text{CaCrO}_4\text{-Iso}(\text{s})}} \\ &= \frac{a_{\text{Ca}^{2+}} \cdot (0.9 \cdot a_{(\text{CrO}_4^{2-})_{\text{bulk}}})^{0.9} \cdot (0.1 \cdot a_{(\text{CrO}_4^{2-})_{\text{bulk}}})^{0.1}}{a_{\text{CaCrO}_4\text{-Iso}(\text{s})}} \\ &= K_{\text{CaCrO}_4} \cdot 0.72 \end{aligned} \quad (31)$$

where  $a_x$  refers to the activity of  $\text{Ca}^{2+}$ , bulk  $\text{CrO}_4^{2-}$ ,  $(^{52}\text{CrO}_4)^{2-}$ ,  $(^{53}\text{CrO}_4)^{2-}$ , bulk  $\text{CaCrO}_4$  and  $^{52}\text{Cr}$ - and  $^{53}\text{Cr}$ -bearing chromatite, and  $\nu_{^{52}\text{Cr}}$  and  $\nu_{^{53}\text{Cr}}$  are the stoichiometric coefficients of  $(^{52}\text{CrO}_4)^{2-}$  and  $(^{53}\text{CrO}_4)^{2-}$  in reaction m5 ( $\approx 0.9$  and  $0.1$ ). Assuming  $\text{CrO}_4^{2-}\text{-bulk} = (^{52}\text{CrO}_4)^{2-} + (^{53}\text{CrO}_4)^{2-}$ ,  $K_{\text{CaCrO}_4}$ , and  $K_{\text{CaCrO}_4\text{-Iso}}$  differ for a given bulk Cr(VI) concentration such as illustrated with Eq. 31. In other words, the solubility of bulk  $\text{CrO}_4^{2-}$  is not the same if the same value is specified for  $K_{\text{CaCrO}_4}$  and  $K_{\text{CaCrO}_4\text{-Iso}}$ . Consequently, the equilibrium constants for  $^{52}\text{Cr}$ - and  $^{53}\text{Cr}$ -bearing jarosite and chromatite (m5 and m6, Table 4) have to be

updated to ensure the same bulk Cr(VI) solubility as for level #3:

$$K_{\text{CaCrO}_4\text{-Iso}} = K_{\text{CaCrO}_4} \cdot (f_{^{52}\text{Cr}})^{\nu_{^{52}\text{Cr}}} \cdot (f_{^{53}\text{Cr}})^{\nu_{^{53}\text{Cr}}} \quad (32)$$

$$K_{\text{Cr-jarosite-Iso}} = K_{\text{Cr-jarosite}} \cdot (f_{^{52}\text{Cr}})^{\nu_{^{52}\text{Cr}}} \cdot (f_{^{53}\text{Cr}})^{\nu_{^{53}\text{Cr}}} \quad (33)$$

$K_{\text{CaCrO}_4}$  and  $K_{\text{Cr-Jarosite}}$  correspond to the equilibrium constants of bulk  $\text{CaCrO}_4$  and bulk jarosite such as used for problem level #3 (m3 and m4, Table 3),  $f_{^{52}\text{Cr}}$  and  $f_{^{53}\text{Cr}}$  refer to the normalized fraction of  $^{52}\text{Cr}$  and  $^{53}\text{Cr}$  (depending on  $\delta^{53}\text{Cr}_{\text{SRM979}}$ ), and  $\nu_{^{52}\text{Cr}}$  and  $\nu_{^{53}\text{Cr}}$  are the stoichiometric coefficients of  $(^{52}\text{CrO}_4)^{2-}$  and  $(^{53}\text{CrO}_4)^{2-}$  in reactions m5 and m6.

It should be noted, that in contrast to the other codes, the jarosite and  $\text{CaCrO}_4$   $\log(K)$  adjustments (32 and 33) are not required using MIN3P. It is not necessary because MIN3P computes mineral solubilities and aqueous kinetic reactions (13 and 14) based on bulk Cr(VI) concentrations.

**Cr(OH)<sub>3</sub>** The solubility of bulk  $\text{Cr}^{3+}$  ( $\text{Cr}^{3+} = (^{52}\text{Cr})^{3+} + (^{53}\text{Cr})^{3+}$ ) remains constant when adding the fate of  $^{52}\text{Cr}$  and  $^{53}\text{Cr}$  to the simulations because the same  $\log(K)$  is specified for bulk  $\text{Cr}(\text{OH})_3$  as well as for the corresponding solid solution end-members (reactions m1, m7 and m8, Table 4).

## 4 Detailed specification of the four problem levels

### 4.1 Level #1: Cr(VI) reduction along a 1D flow path

The simulation is carried out for a 1D flow path of 800 m to track Cr(VI) reduction along a large concentration range. The model domain is discretized into 800 cubical grid blocks with a dimension of  $1 \times 1 \times 1$  m each. The simulation is run for 1,000 days. The porosity is set to a fixed value of 0.17 for the whole model domain (i.e., no porosity update due to mineral dissolution and precipitation reactions). A constant flux boundary condition is specified for the two model boundaries by assigning an injection rate of  $6.887 \times 10^{-3}$  kg/s into the upstream boundary grid block and an extraction rate of  $-6.887 \times 10^{-3}$  kg/s out of the downstream boundary grid block. For a porosity of 0.17 and the specified model domain this injection rate corresponds to a fixed (i.e., constant) average linear flow velocity of 3.5 m/day, which is in agreement with the inferred

groundwater flow velocity along the best constrained flow path at the Riviera site [18].

The diffusion coefficient is set to  $10^{-9}$  m<sup>2</sup>/s. The approaches for simulating hydrodynamic dispersion differs between the different codes used to solve this benchmark [41]. Using CRUNCHFLOW, MIN3P, and FLOTRAN hydrodynamic dispersion is simulated by means of a dispersion tensor. By contrast, TOUGHREACT requires the accurate definition of aquifer heterogeneity to simulate hydrodynamic dispersion, which often requires the specification of a multicontinuum [51]. Due to the different treatments, a good match between the codes is challenging for problems involving hydrodynamic dispersion. Accordingly, we did not consider hydrodynamic dispersion for this particular benchmark. In fact, we postulate that matching hydrodynamic dispersion using these four codes would serve as a benchmark of its own.

With the exception of the upstream boundary grid block, initial total concentrations are defined according to major cation and anion concentrations measured in an uncontaminated groundwater sample (Table 5, [18]). For the upstream boundary grid block, aqueous concentrations are kept constant (fixed boundary condition, see Table 5). They are

**Table 5** Initial (levels #1-4) and boundary primary species concentration (levels #1-2) used for the four problem levels

	Unit	Initial concentration (total conc.)	Fixed boundary concentration (total conc.)
pH		6.2	6.2
Na <sup>+</sup>	mg/L	4.7	4.7
K <sup>+</sup>	mg/L	0.9	0.9
Mg <sup>2+</sup>	mg/L	2	2
Ca <sup>2+</sup>	mg/L	13.58	13.58
Cl <sup>-</sup>	mg/L	<sup>1</sup> 18.77	<sup>1</sup> 18.66
SO <sub>4</sub> <sup>2-</sup>	mg/L	8.85	8.85
NO <sub>3</sub> <sup>-</sup>	mg/L	12.25	12.25
HCO <sub>3</sub> <sup>-</sup>	mg/L	22.58	22.58
CrO <sub>4</sub> <sup>2-</sup>	mg/L	0	0.08 <sup>2</sup>
Fe <sup>2+</sup>	mg/L	0.01	0.01
Fe <sup>3+</sup>	mg/L	0	0
SiO <sub>2(aq)</sub>	mg/L	0	0
Cr <sup>3+</sup>	mg/L	0	0
Al <sup>3+</sup>	mg/L	0	0

<sup>1</sup>Obtained by employing a charge balance constraint. The measured concentration was 13.2 mg/L

<sup>2</sup>For component problem #2, this concentration was assigned to <sup>52</sup>(CrO<sub>4</sub>)<sup>2-</sup> 1.39373917E-6 mol/kgH<sub>2</sub>O and <sup>53</sup>(CrO<sub>4</sub>)<sup>2-</sup> (1.58038813E-7 mol/kgH<sub>2</sub>O) to specify an initial  $\delta^{53}\text{Cr}_{\text{SRM979}}$  of 0.0 ‰

specified according to a chemical analysis of a typical Cr(VI) contaminated groundwater sample with a Cr(VI) concentration of 0.08 mg/L (Table 5).

The reaction network used for problem level #1 is composed of aqueous reactions a1—a36, mineral reactions m1, m2, and m9–m11 (Tables 2 and 3) and the aqueous kinetic reaction reducing Cr(VI) to Cr(III) (5 and 6). The following initial mineral volume fractions are assigned to the whole model domain: 68 % quartz, 10 % annite, 4 % chamosite, 1 % CO<sub>2(s)</sub>, and 0.0 % Cr(OH)<sub>3(am)</sub> (% of entire porous medium). CO<sub>2(s)</sub> is a hypothetical phase that was used to fix the log(*p*CO<sub>2</sub>) to -1.7 by specifying a large reaction rate constant and by setting log(K) to -9.5 (Table 4). A log(*p*CO<sub>2</sub>) of -1.7 corresponds to the observation that the calculated CO<sub>2</sub> partial pressures of groundwater samples were more or less uniform and close to this value [18].

#### 4.2 Level #2: simulation of Cr isotopic fractionation for the 1D problem

This problem level adds Cr isotope fractionation to level #1 using the same initial specification to simulate flow and transport. The only exception is that the Cr(VI) concentration of the upstream boundary (0.08 mg/L, Table 5) is assigned to (<sup>52</sup>CrO<sub>4</sub>)<sup>2-</sup> and (<sup>53</sup>CrO<sub>4</sub>)<sup>2-</sup> instead of the bulk CrO<sub>4</sub><sup>2-</sup> taking into account the normalized bulk earth fraction of <sup>52</sup>Cr and <sup>53</sup>Cr, which are 0.89815629 and 0.1018437, respectively [49]. In doing so, inlet (<sup>52</sup>CrO<sub>4</sub>)<sup>2-</sup> and (<sup>53</sup>CrO<sub>4</sub>)<sup>2-</sup> concentration are fixed to 1.39373917E-6 and 1.58038813E-7 mol/kgH<sub>2</sub>O while the total Cr(VI) concentration (<sup>52</sup>CrO<sub>4</sub>)<sup>2-</sup> + (<sup>53</sup>CrO<sub>4</sub>)<sup>2-</sup>) remains at the same concentration as specified for problem level #1 (1.551778e-6 mol/kg = 0.08 mg/L, Table 5). According to Eq. 7, this definition yields an initial  $\delta^{53}\text{Cr}_{\text{SRM979}}$  value of 0.0 ‰.

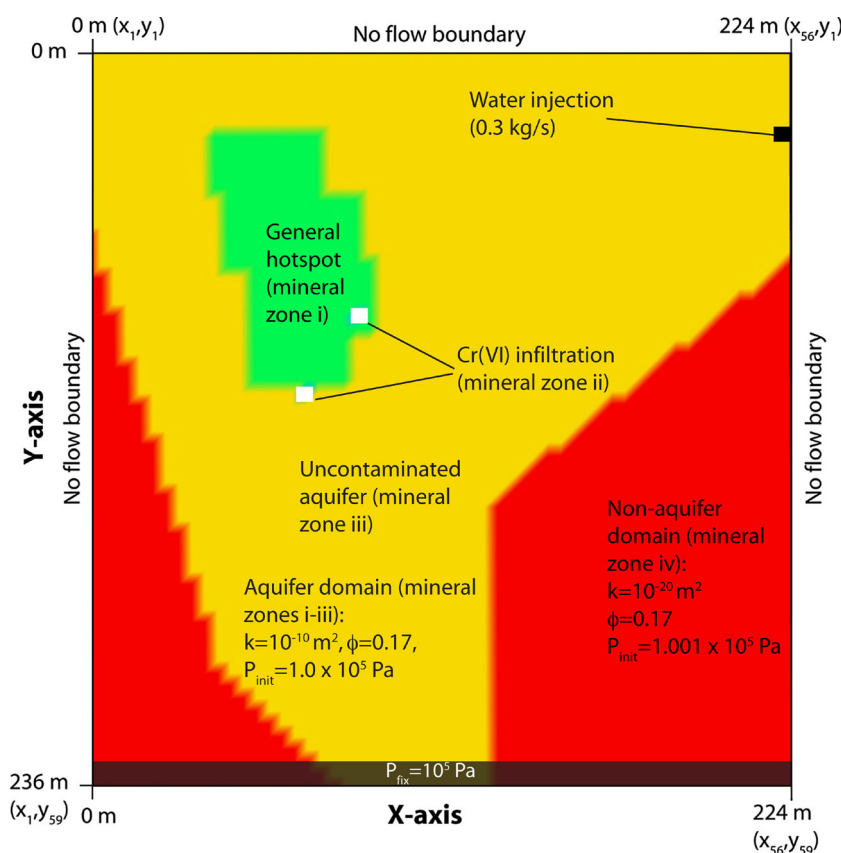
The reaction network used in this simulation is composed of aqueous reactions a1—a36 (Table 2) and mineral reactions m2 and m7–m11 (Table 3), as well as the aqueous kinetic reactions simulating the reduction of (<sup>52</sup>CrO<sub>4</sub>)<sup>2-</sup> and (<sup>53</sup>CrO<sub>4</sub>)<sup>2-</sup> to (<sup>52</sup>Cr)<sup>3+</sup> and (<sup>53</sup>Cr)<sup>3+</sup>, respectively (8–14).

#### 4.3 Level #3: simulation of 2D Cr(VI) plume

The 2D flow field is adapted from a previous hydrological flow simulation performed by a consulting company using the software “Groundwater Modeling System” (GMS). A domain of 224 × 236 m is used. It is discretized into 56 × 59 cubical grid blocks having a dimension of 4 × 4 × 1 m each and the simulation is run for 1,000 days.

The model domain is divided into two different flow domains (Fig. 2). The first domain, labeled as aquifer

**Fig. 2** 2D domain for the simulation of problem levels #3 and #4 illustrating the actual aquifer domain and the location of the different mineral zones as well as initial and boundary conditions for setting up the steady state flow field



domain, corresponds to the actual aquifer and consists of mineral zones i–iii such as defined below. The second domain, labeled as non-aquifer domain, corresponds to the part of the rectangular 2D domain where no aquifer is present and consists of mineral zone iv. Permeability and porosity of the aquifer domain are set to fixed values of  $10^{-10} \text{ m}^2$  and 0.17, whereas a permeability of  $10^{-20} \text{ m}^2$  and the same porosity (0.17) is used for the non-aquifer domain. The aquifer domain comprises grid blocks except the ones with the  $x, y$ -coordinates (i.e.,  $x_m, y_n$ ) listed in Table 6 (Fig. 2).

An initial fluid pressure of  $1.0 \times 10^5 \text{ Pa}$  is specified for the whole model domain. No-flow boundary conditions are defined for the  $x$ -begin ( $x_m, y_1$ ),  $y$ -begin ( $x_1, y_m$ ), and  $y$ -end ( $x_{56}, y_n$ ) boundary. For the  $x$ -end boundary ( $x_m, y_{59}$ ), a flux boundary condition is specified by fixing the fluid pressure to  $1 \times 10^5 \text{ Pa}$ . The aquifer at the site is mainly fed by meteoric water originating from precipitations along the adjacent mountain ranges. To mimic this observation, a constant water injection rate of 0.3 kg/s is defined for grid block  $x_{56}, y_7$  (Fig. 2).

As for the two 1D levels, the diffusion coefficient is set to  $10^{-9} \text{ m}^2/\text{s}$  and hydrodynamic dispersion was not considered. The same initial total aqueous species concentrations as for problem level #1 is specified for the whole model

domain (Table 5). For the water injection grid block ( $x_{56}, y_7$ ), total aqueous species concentrations are fixed for the entire simulation.

The reaction network used in this simulation is composed of aqueous complexation reactions a1–a36 (Table 2), mineral reactions m1–m4 and m9–m11 (Table 3), and the

**Table 6** Grid blocks belonging to the non-aquifer domain (Fig. 2)

(x <sub>1</sub> ,y <sub>15–59</sub> )	(x <sub>16</sub> ,y <sub>55–59</sub> )	(x <sub>43</sub> ,y <sub>29–59</sub> )
(x <sub>2</sub> ,y <sub>19–59</sub> )	(x <sub>17</sub> ,y <sub>56–59</sub> )	(x <sub>44</sub> ,y <sub>28–59</sub> )
(x <sub>3</sub> ,y <sub>22–59</sub> )	(x <sub>18</sub> ,y <sub>57–59</sub> )	(x <sub>45</sub> ,y <sub>27–59</sub> )
(x <sub>4</sub> ,y <sub>26–59</sub> )	(x <sub>19</sub> ,y <sub>58–59</sub> )	(x <sub>46</sub> ,y <sub>26–59</sub> )
(x <sub>5</sub> ,y <sub>29–59</sub> )	(x <sub>20</sub> ,y <sub>59</sub> )	(x <sub>47</sub> ,y <sub>25–59</sub> )
(x <sub>6</sub> ,y <sub>32–59</sub> )	(x <sub>33</sub> ,y <sub>37–59</sub> )	(x <sub>48</sub> ,y <sub>25–59</sub> )
(x <sub>7</sub> ,y <sub>36–59</sub> )	(x <sub>34</sub> ,y <sub>36–59</sub> )	(x <sub>49</sub> ,y <sub>24–59</sub> )
(x <sub>8</sub> ,y <sub>39–59</sub> )	(x <sub>35</sub> ,y <sub>35–59</sub> )	(x <sub>50</sub> ,y <sub>23–59</sub> )
(x <sub>9</sub> ,y <sub>43–59</sub> )	(x <sub>36</sub> ,y <sub>34–59</sub> )	(x <sub>51</sub> ,y <sub>22–59</sub> )
(x <sub>10</sub> ,y <sub>46–59</sub> )	(x <sub>37</sub> ,y <sub>34–59</sub> )	(x <sub>52</sub> ,y <sub>21–59</sub> )
(x <sub>11</sub> ,y <sub>50–59</sub> )	(x <sub>38</sub> ,y <sub>33–59</sub> )	(x <sub>53</sub> ,y <sub>21–59</sub> )
(x <sub>12</sub> ,y <sub>51–59</sub> )	(x <sub>39</sub> ,y <sub>32–59</sub> )	(x <sub>54</sub> ,y <sub>20–59</sub> )
(x <sub>13</sub> ,y <sub>52–59</sub> )	(x <sub>40</sub> ,y <sub>31–59</sub> )	(x <sub>55</sub> ,y <sub>19–59</sub> )
(x <sub>14</sub> ,y <sub>53–59</sub> )	(x <sub>41</sub> ,y <sub>30–59</sub> )	(x <sub>56</sub> ,y <sub>18–59</sub> )
(x <sub>15</sub> ,y <sub>54–59</sub> )	(x <sub>42</sub> ,y <sub>30–59</sub> )	

aqueous kinetic reaction between aqueous Cr(VI) and Fe(II) (5 and 6). In the case of jarosite, the reaction network includes dissolution only. Jarosite precipitation was suppressed because jarosite is typically formed under highly acidic conditions [55]. Four different initial mineral zones were defined within the model domain (Fig. 2): (i) a general hotspot domain with 67.72 % quartz, 10 % annite, 4 % chamosite, 0.3 % Cr(VI)-bearing jarosite (e.g., Cr-Jarosite), 1 % CO<sub>2</sub>(s), and 0.0 % Cr(OH)<sub>3(am)</sub> (% of entire porous medium). This zone was assigned to the following grid blocks (Fig. 2): ( $x_{11-19}, y_{8-13}$ ), ( $x_{12-19}, y_{13-18}$ ), ( $x_{14-20}, y_{18-23}$ ), ( $x_{14-21}, y_{23-27}$ ), ( $x_{20-22}, y_{13-18}$ ), and ( $x_{21-23}, y_{18-23}$ ) except ( $x_{22}, y_{22}$ ). (ii) The second, small zone (two grid blocks, “Cr(VI) infiltration”) simulates the vertical infiltration of a high Cr(VI) load derived from the dissolution of highly soluble Cr(VI) phases (e.g., chromate (CaCrO<sub>4</sub>)) accumulated in the saturated zone [18]. It is assigned to grid blocks ( $x_{18}, y_{28}$ ) and ( $x_{22}, y_{22}$ ) (Fig. 2) and contained 65 % quartz, 10 % annite, 4 % chamosite, 3 % chromate (CaCrO<sub>4</sub>) 1 % CO<sub>2</sub>(s), and 0.0 % Cr(OH)<sub>3(am)</sub> (% of entire porous medium). (iii) The initial mineral phase distribution of the remaining part of the aquifer domain (mineral zone iii) is the same as for problem level #1 (68 % quartz, 10 % annite, 4 % chamosite and 1 % CO<sub>2</sub>(s) and corresponds to the uncontaminated aquifer. (iv) The same initial mineralogical composition as for mineral zone iii was assigned to the non-aquifer domain.

#### 4.4 Level #4: simulation of Cr isotopic fractionation for the 2D problem

This level adds Cr isotope fractionation to level #3 using the same initial specification to simulate flow and transport. The reaction network is composed of aqueous complexation reactions a1–a36 (Table 2), mineral reactions m2 and m5–m11 (Table 3), and aqueous kinetic reactions simulating the reduction of (<sup>52</sup>CrO<sub>4</sub>)<sup>2-</sup> and (<sup>53</sup>CrO<sub>4</sub>)<sup>2-</sup> to (<sup>52</sup>Cr)<sup>3+</sup> and (<sup>53</sup>Cr)<sup>3+</sup>, respectively (8–14). The same initial mineral zone distribution as for level #3 is used (Fig. 2). Also, the assigned initial mineral volume fractions are the same except that Cr-Jarosite is replaced by “Cr-Jarosite-Iso” and CaCrO<sub>4(s)</sub> is replaced by “CaCrO<sub>4(s)</sub>-Iso” (reactions m5 and m6, Table 3). As for level #3, jarosite precipitation is suppressed. With this specification, the two Cr(VI) isotopologues are introduced to the aqueous phase by dissolution of “CaCrO<sub>4</sub>-Iso” and “Cr-Jarosite-Iso” (Table 3). By using a ratio of the stoichiometric coefficients of (<sup>52</sup>CrO<sub>4</sub>)<sup>2-</sup> and (<sup>53</sup>CrO<sub>4</sub>)<sup>2-</sup> that is equal to the ratio of the bulk earth distribution (<sup>53</sup>Cr/<sup>52</sup>Cr = 0.11339, Table 3) and a sufficiently high reaction rate constant (Table 4) to establish equilibrium for these two minerals the model assumes a source  $\delta^{53}\text{Cr}_{\text{SRM979}}$  value of 0.0 ‰. Assuming  $\delta^{53}\text{Cr}_{\text{SRM979}} = 0.0 \text{ ‰}$  is based on the observation

that anthropogenic Cr(VI) sources (e.g., chromic acid) generally show  $\delta^{53}\text{Cr}_{\text{SRM979}}$  values close to 0.0 ‰ [17, 20]. Partial Cr(VI) reduction prior CaCrO<sub>4</sub> and jarosite formation could have shifted the corresponding  $\delta^{53}\text{Cr}_{\text{SRM979}}$  to higher values. However, due to the absence of  $\delta^{53}\text{Cr}_{\text{SRM979}}$  measurements for pure CaCrO<sub>4</sub> and jarosite such an effect on  $\delta^{53}\text{Cr}_{\text{SRM979}}$  was not considered. According to Eqs. 32–33 and by assuming  $\delta^{53}\text{Cr}_{\text{SRM979}} = 0.0 \text{ ‰}$ , log(K) of jarosite and CaCrO<sub>4</sub> (m5 and m6, Table 4) are updated to  $-8.74293$  (CaCrO<sub>4(s)</sub>-Iso) and  $-12.02859$  (Cr-Jarosite-Iso) to ensure the same bulk Cr(VI) solubility as for level #3.

## 5 Results and discussion

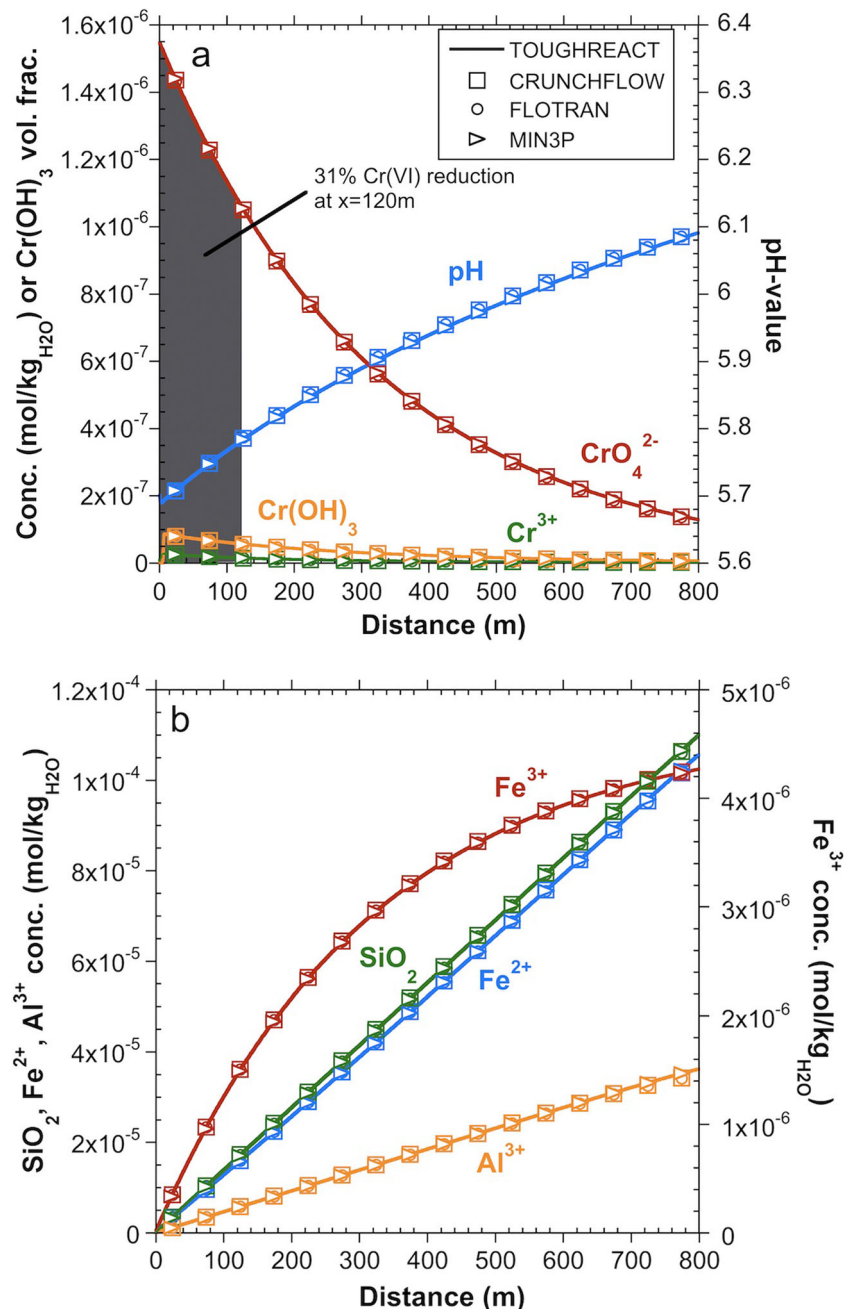
### 5.1 Level #1

#### 5.1.1 General simulation results

Steady state spatial profiles of total aqueous species concentrations involved in Cr(VI) reduction (5) are shown in Fig. 3 together with total Al<sup>3+</sup> and SiO<sub>2</sub> concentrations, pH value, and precipitated Cr(OH)<sub>3</sub> volume fraction profiles. Dissolved Fe<sup>2+</sup> required for Cr(VI) reduction (5) was inherited by annite and chamosite dissolution inducing a continuous increase of SiO<sub>2</sub> and Al<sup>3+</sup> along the 1D model domain. The observation that Fe<sup>2+</sup> also increased linearly along the model domain illustrates that for the given (i.e., large) total ferrous iron concentrations, Fe<sup>2+</sup> is not significantly affected by Cr(VI) reduction (5) and that chamosite and annite dissolution rates have a strong control on total Fe<sup>2+</sup> concentration. It should be noted that for annite a reaction rate constant larger than the one reported by Palandri and Kharaka [56] was used (Table 4) to obtain similar Fe<sup>2+</sup> concentrations as observed in the field (ca. 2 mg/L [18]). Therefore, specified annite dissolution rates do not represent “true” field scale rates, but rather form a (simplified) way of obtaining redox conditions (e.g., Fe<sup>2+</sup> concentrations), similar to the ones observed in the field. Moreover, the specified annite dissolution rate ensures that Fe<sup>2+</sup> is available in excess of Cr(VI), thus justifying the definition of a first-order dependence of the Cr(VI) reduction rate on the total Cr(VI) concentration (6).

Due to its low solubility, aqueous Cr<sup>3+</sup> formed by Eq. 5 precipitated as amorphous Cr(OH)<sub>3</sub> yielding low total dissolved Cr<sup>3+</sup> concentrations on the order of 1e-8 mol/kgH<sub>2</sub>O or lower (Fig. 3a). With the specified reaction network, about 90 % of the inlet Cr(VI) concentration was reduced along the simulated flow path. The extent of Cr(VI) reduction at  $x = 120 \text{ m}$  was ca. 31 % such as inferred for the field site [18]. Chlorine evolution at the downstream model boundary ( $x = 800 \text{ m}$ ) show that the breakthrough of

**Fig. 3** Steady state profiles of various components obtained for level #1 after a simulated time period of 1,000 days. **a** Total Cr(VI) and Cr(III) concentration, pH value, and Cr(OH)<sub>3</sub> volume fraction profiles. The *gray shaded domain* illustrates that 31 % of the initial Cr(VI) is reduced after a flow path of 120 m, such as inferred for the field site [18]. **b** Total Fe(II), Fe(III), SiO<sub>2(aq)</sub>, and Al<sup>3+</sup> concentration profiles



the influent solution (Table 5) occurred after ca. 230 days (Fig. 4) confirming that the simulation was run at an average linear flow velocity of 3.5 days.

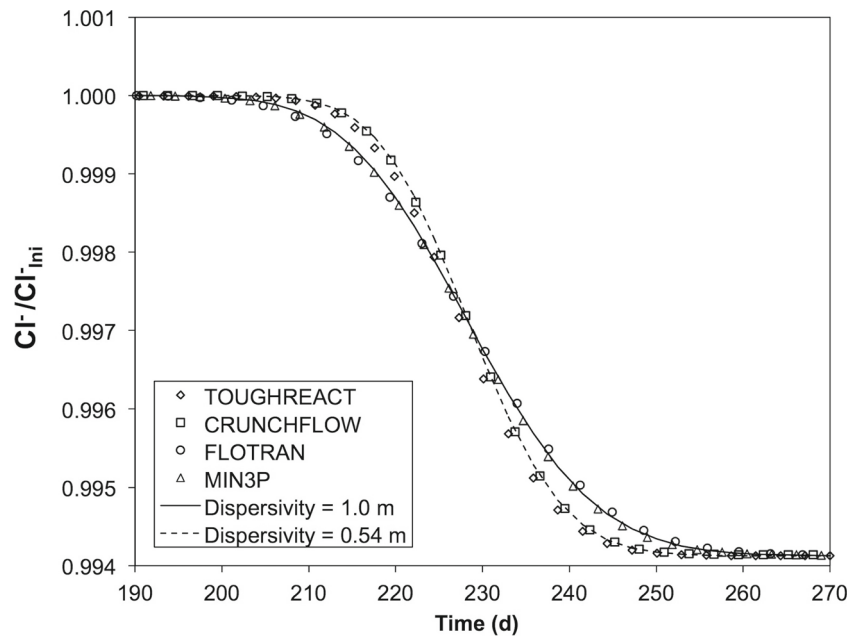
### 5.1.2 Code comparison

Results obtained from different codes match each other almost perfectly (Fig. 3). The only minor differences were observed for the breakthrough curves (Fig. 4). By neglecting hydrodynamic dispersion, these breakthrough curves are solely inherited from numerical dispersion. Accordingly,

the minor breakthrough curve variations illustrate that the different numerical approaches for solving transport introduced a slightly variable degree of numerical dispersion. The numerical dispersion coefficient  $D_n$  and corresponding numerical dispersivity ( $D_n/v$ ) was estimated using an analytical solution [57] for the time dependent Cl<sup>-</sup> concentration at the downstream model boundary ( $x = 800$  m):

$$c(t)_{x=800 \text{ m}} = c_{\text{ini}} + \frac{c_{\text{boun}} - c_{\text{init}}}{2} \operatorname{erfc} \left( \frac{800 - vt}{\sqrt{(4D_n t)}} \right) \quad (34)$$

**Fig. 4** Temporal evolution of the total  $\text{Cl}^-$  concentration at the downstream model boundary ( $x = 800$  m) for level #1 around the time of breakthrough. Also shown are analytical breakthrough curves for dispersivities of 0.54 and 1.0 m, respectively. By neglecting hydrodynamic dispersion, these dispersivities are solely inherited from numerical dispersion



where  $c_{ini}$  and  $c_{bound}$  refer to the initial and boundary  $\text{Cl}^-$  concentrations,  $v$  is the average linear flow velocity,  $D_n$  refers to the numerical dispersion coefficient. Applying Eq. 34 to the various breakthrough curves yields numerical dispersivities of 0.54 m (TOUGHREACT and CRUNCHFLOW) and 1.0 m (FLOTRAN, MIN3P), respectively.

It should be noted, that this benchmark does not aim to investigate numerical approaches for simulating transport processes. Accordingly, a discussion regarding numerical approaches to cause variable numerical dispersion is beyond the scope of this paper. For an extended discussion, it is referred to Steefel et al. [41] and references therein.

## 5.2 Level #2

### 5.2.1 The fate of individual Cr isotopes

$\delta^{53}\text{Cr}_{\text{SRM979}}$  value profiles (Fig. 5d) for the three Cr pools of the problem (i.e., dissolved Cr(VI), dissolved Cr(III), and solid  $\text{Cr}(\text{OH})_3$ ) show that the problem entirely follows a Rayleigh-type fractionation model

$$\delta^{53}\text{Cr}_{\text{SRM979},x} = \left[ \left( \delta^{53}\text{Cr}_{\text{SRM979},0} + 1000 \right) \cdot f^{(\alpha-1)} \right] - 1000 \quad (35)$$

where  $\delta^{53}\text{Cr}_{\text{SRM979},x}$  and  $\delta^{53}\text{Cr}_{\text{SRM979},0}$  refer to the  $\delta^{53}\text{Cr}_{\text{SRM979}}$  values at location  $x$  and at the column inlet (0.0 ‰ for Cr(VI) and -3.4 ‰ for Cr(III)),  $f$  refers to the remaining Cr(VI) fraction at location  $x$  and  $\alpha = \alpha^{53}\text{Cr}_{\text{Cr(III)}/\text{Cr(VI)}} = 0.9966$  is the kinetic fractionation factor that was used to simulate Cr isotope fractionation (8–14). Note that  $\delta^{53}\text{Cr}_{\text{SRM979}}$  values of the precipitated

$\text{Cr}(\text{OH})_3$  solid solution were calculated in analogue to the ones for dissolved Cr(VI) and Cr(III) (7) using the computed ratio of the volume fractions of the two isotopic end-members ( $V_{53\text{Cr}(\text{OH})_3} / V_{52\text{Cr}(\text{OH})_3}$ ) and assuming an equal molar volume for both end-members ( $29.09 \text{ cm}^3/\text{mol}$ ):

$$\delta^{53}\text{Cr}_{\text{SRM979}} = \frac{\left( V_{53\text{Cr}(\text{OH})_3} / V_{52\text{Cr}(\text{OH})_3} \right)}{R \left( ^{53}\text{Cr} / ^{52}\text{Cr} \right)_{\text{SRM979}}} - 1 \quad (36)$$

The trend of increasing  $\delta^{53}\text{Cr}_{\text{SRM979}}$  values with decreasing Cr(VI) concentrations illustrate that Cr(VI) reduction is accompanied by an accumulation of the heavy Cr isotopes in the remaining aqueous phases whereas formed  $\text{Cr}^{3+}$  becomes enriched in the lighter Cr isotopes.

### 5.2.2 Code comparison

Simulated total Cr(III) and Cr(VI) concentration profiles of the two Cr(VI) and Cr(III) isotopologues as well as  $^{52}\text{Cr}(\text{OH})_3$  and  $^{53}\text{Cr}(\text{OH})_3$  volume fraction profiles match almost perfectly when comparing results from different codes (Fig. 5a–c). The same applies for the  $\delta^{53}\text{Cr}$  value profiles of the three Cr pools (Fig. 5d). Moreover, for any code ( $^{52}\text{CrO}_4^{2-}$  and  $^{53}\text{CrO}_4^{2-}$  as well as  $(^{52}\text{Cr})^{3+}$  and  $(^{53}\text{Cr})^{3+}$  sum up almost perfectly to the corresponding bulk species (e.g.,  $\text{CrO}_4^{2-}$ ,  $\text{Cr}^{3+}$ ) obtained for level #1 (Fig. 6). The same applies for the steady state  $^{52}\text{Cr}(\text{OH})_3$  and  $^{53}\text{Cr}(\text{OH})_3$  volume fractions, which also sum up to the bulk  $\text{Cr}(\text{OH})_3$  volume fractions obtained for level #1 (Fig. 6).

Our conceptual model assumes that Cr(VI) reduction and accompanying Cr isotopic fractionation is inherited from

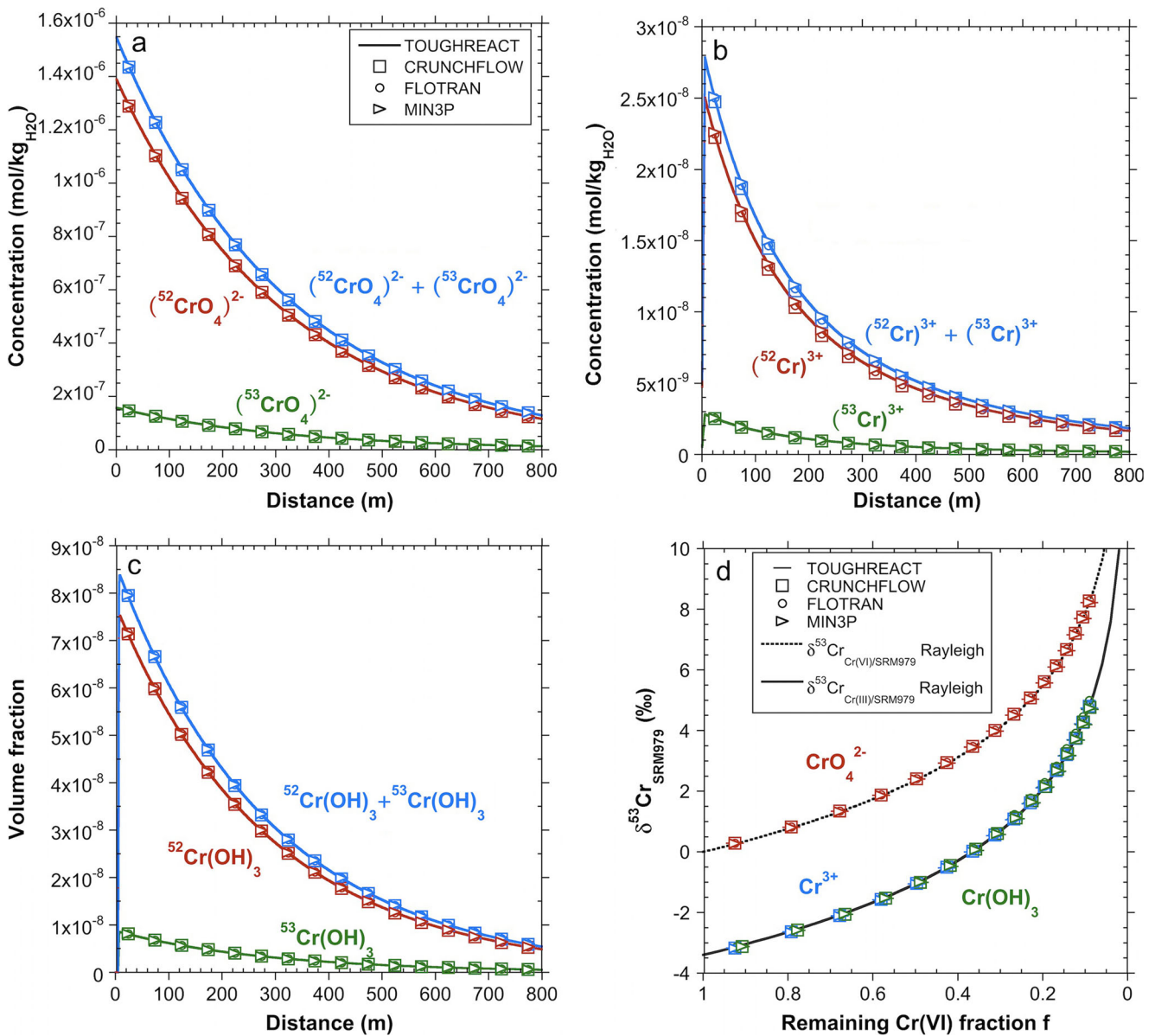


**Fig. 5** Steady state profiles obtained for level #2 for different Cr pools after a simulated time period of 1,000 days. **a** Total  $(^{52}\text{CrO}_4)^{2-}$ ,  $(^{53}\text{CrO}_4)^{2-}$ , and  $(^{52}\text{CrO}_4)^{2-} + (^{53}\text{CrO}_4)^{2-}$  concentration profiles. **b** Total  $(^{52}\text{Cr})^{3+}$ ,  $(^{53}\text{Cr})^{3+}$ , and  $(^{52}\text{Cr})^{3+} + (^{53}\text{Cr})^{3+}$  concentration profiles. **c**  $^{52}\text{Cr}(\text{OH})_3$ ,  $^{53}\text{Cr}(\text{OH})_3$ , and  $^{52}\text{Cr}(\text{OH})_3 + ^{53}\text{Cr}(\text{OH})_3$  volume fraction profiles. **d** Steady state  $\delta^{53}\text{Cr}_{\text{SRM979}}$  values for dissolved  $\text{CrO}_4^{2-}$  and  $\text{Cr}^{3+}$  as well as for precipitated  $\text{Cr}(\text{OH})_3$

as a function of the remaining Cr(VI) fraction  $f$  (open symbols). Also illustrated are Rayleigh-type fractionation models (Eq. 35) with  $\alpha^{53}\text{Cr}_{\text{Cr(III)/Cr(VI)}} = 0.9966$  for Cr(VI) ( $\delta^{53}\text{Cr}_{\text{Cr(VI)/SRM979}}$ ) and Cr(III) ( $\delta^{53}\text{Cr}_{\text{Cr(III)/SRM979}}$ ), which perfectly match the three simulated Cr pools. The observation that  $\text{Cr}^{3+}$  and  $\text{Cr}(\text{OH})_3$  both plot on  $\delta^{53}\text{Cr}_{\text{Cr(III)/SRM979}}$  illustrates that no fractionation was induced by  $\text{Cr}(\text{OH})_3$  precipitation

a first-order irreversible aqueous reaction where the reaction product is removed from the solution (Fig. 1). Since these are the main characteristics of a Rayleigh distillation process, the good fit with the analytical Rayleigh equation (Fig. 5d) adds additional confidence to the simulation results. In particular, the good match between the steady state  $\delta^{53}\text{Cr}_{\text{SRM979}}$  profiles of dissolved  $\text{Cr}^{3+}$  and the ones for precipitated  $\text{Cr}(\text{OH})_3$  confirms that Cr isotope

fractionation was solely accomplished during reduction of Cr(VI) to Cr(III), and no fractionation occurred during precipitation of  $\text{Cr}(\text{OH})_3$ . The good agreement among different codes is especially notable given that the implementation of Cr isotope fractionation is different in different codes (see 10–29).

It should be noted, however, that the good match between the simulation results and the Rayleigh equation is only

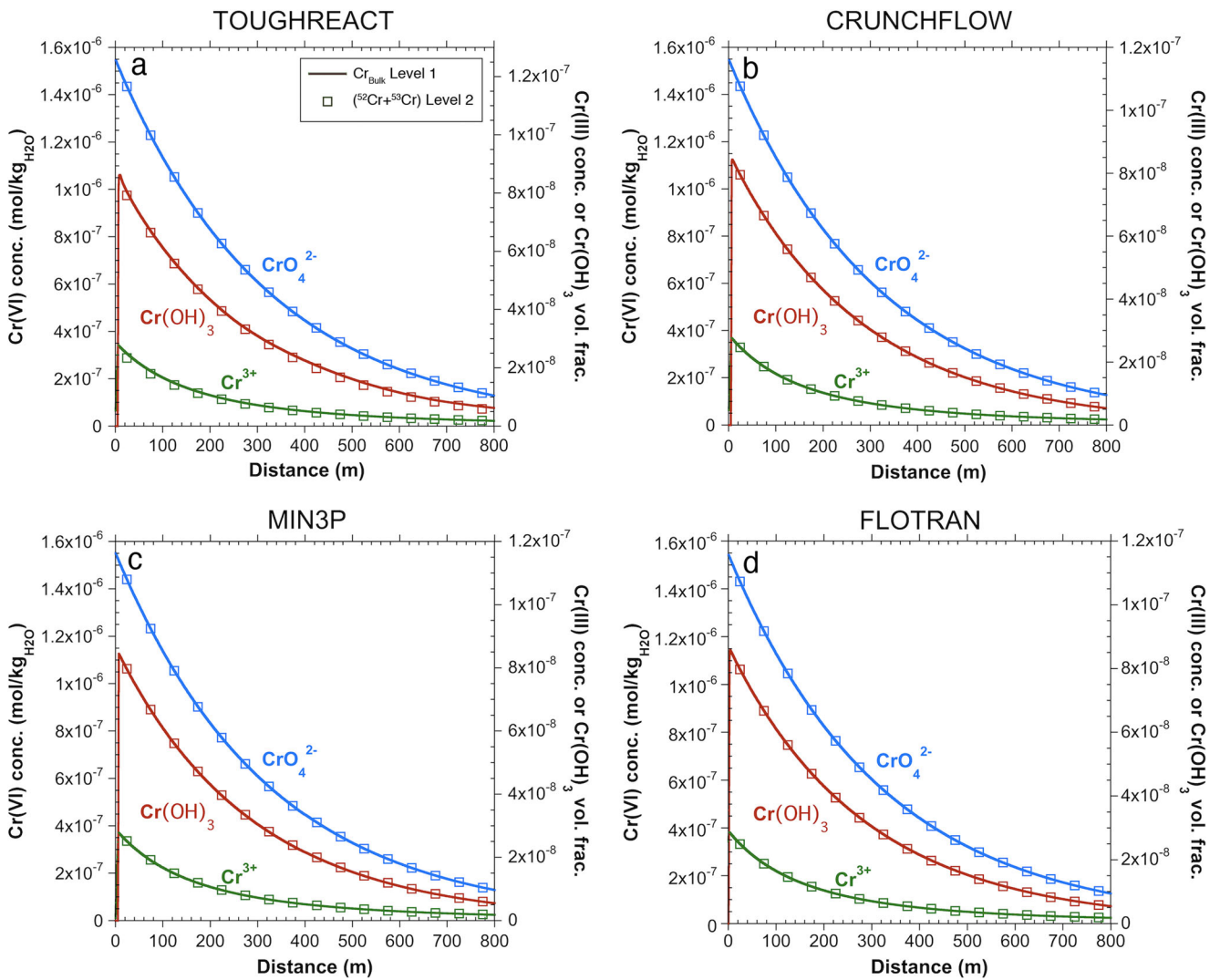


**Fig. 6** Comparison between total bulk Cr(VI) and Cr(III) concentration and bulk Cr(OH)<sub>3</sub> volume fraction profiles obtained for levels #1 and #2 using different codes. **a** TOUGHREACT, **b** CRUNCHFLOW, **c** MIN3P, and **d** FLOTTRAN

obtained because hydrodynamic dispersion was not considered. This limitation occurs because a system’s effective fractionation factor is shifted to a value closer to unity (less fractionation) if the Cr(VI) reduction rate is transport-limited [21] or if strong hydrodynamic dispersion is occurring [27, 28]. Accordingly, for substantial longitudinal dispersion, we expect that a well-fitting Rayleigh model would require a fractionation factor closer to unity (less fractionation) than defined as input parameter ( $\alpha = 0.9966$ ).

### 5.3 Level #3

#### 5.3.1 General simulation results

Steady state total  $\text{CrO}_4^{2-}$  concentrations (Fig. 7a) demonstrate that the overall Cr(VI) plume in the aquifer is largely dominated by the dissolution of chromate (CaCrO<sub>4</sub>)

present in the Cr(VI) infiltration zone (Fig. 2). By contrast, steady state total  $\text{CrO}_4^{2-}$  concentrations were significantly lower in the general hotspot domain (Fig. 7a). These variable Cr(VI) concentrations are inherited by a much higher chromate solubility when compared to the solubility of jarosite (Table 4). Owing to the specified high reaction rate constant (Table 4), saturation with respect to jarosite is quickly established, thus forming a solubility control on the Cr(VI) plume. The strong Cr(VI) concentration contrast between the two hotspot domains in turn illustrates that the environmental hazards of Cr(VI) contaminations are strongly controlled by the mineralogical composition of Cr(VI) hotspots.

The dissolution of jarosite introduces elevated total  $\text{Fe}^{3+}$  and  $\text{SO}_4^{2-}$  concentrations to the aquifer in addition to the Cr(VI) plume (Fig. 7e–f). The steady state total  $\text{Fe}^{3+}$  concentrations, however, are also affected by Cr(VI) reduction,

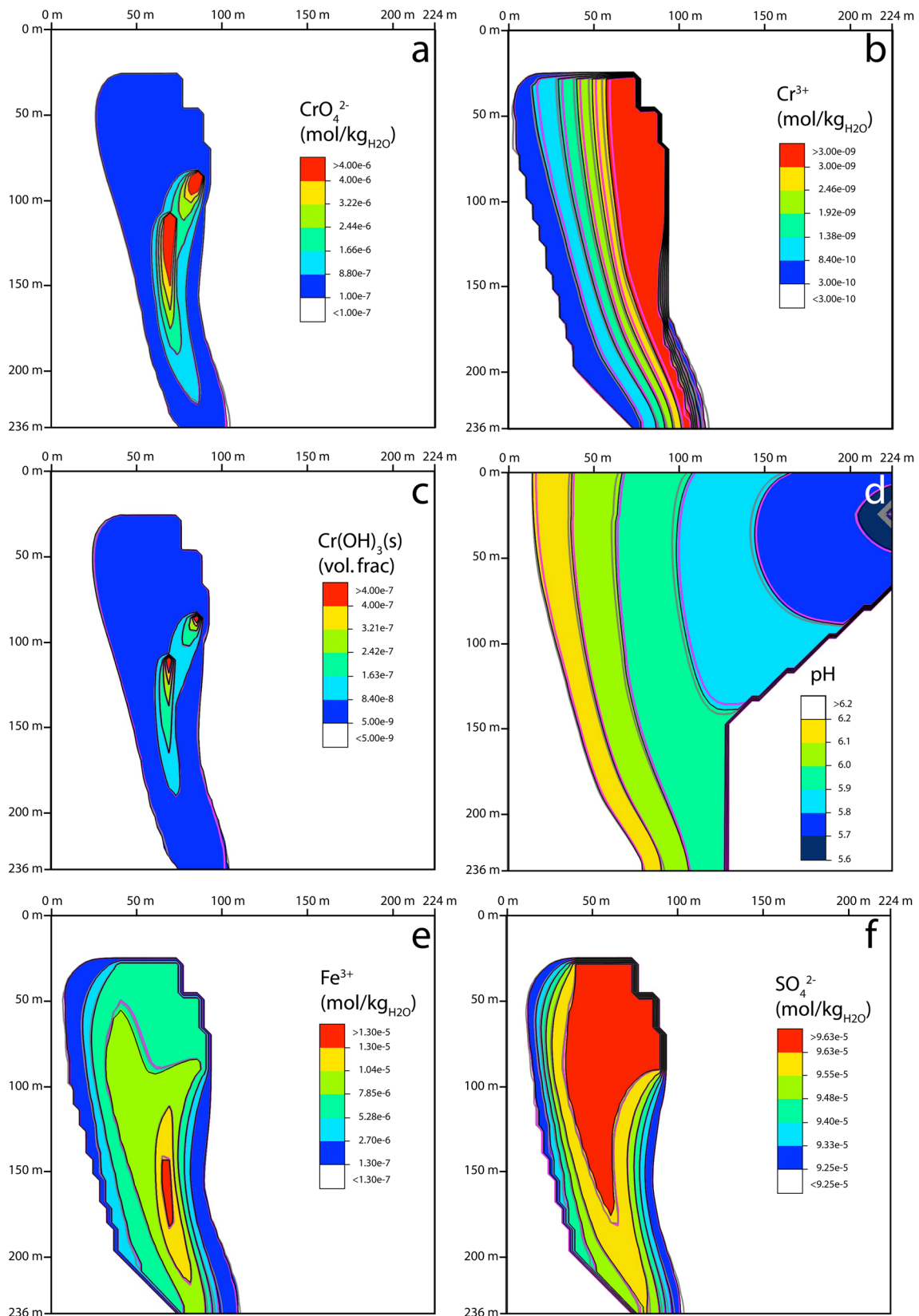


**Fig. 7** Steady state spatial distribution of selected total aqueous species concentrations,  $\text{Cr(OH)}_3$  volume fractions, and fluid pressure obtained for level #3 after a simulated time of 1,000 days. The colors

and black contours indicate results obtained from the TOUGHREACT runs. MIN3P and CRUNCHFLOW results are shown as gray and purple contour lines, respectively

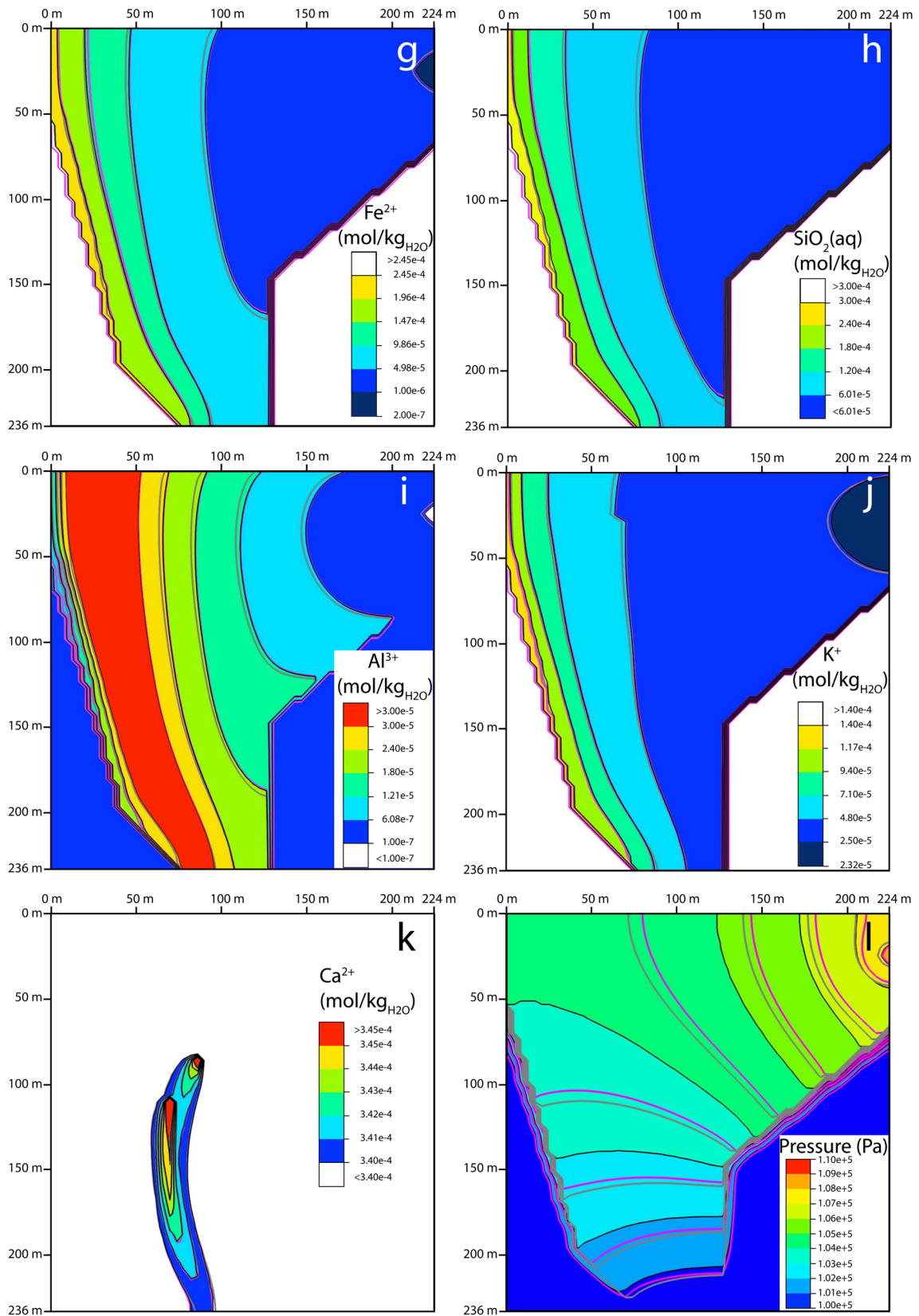


Fig. 7 (continued)

which produces  $\text{Fe}^{3+}$  in addition to  $\text{Cr}^{3+}$  (5). Accordingly, the second domain with elevated total  $\text{Fe}^{3+}$  concentrations is observed near the Cr(VI) infiltration zones in addition to the one generated by jarosite dissolution. The highest total  $\text{Fe}^{3+}$  concentrations are found slightly downstream of the second (i.e., downstream) Cr(VI) infiltration zone where both  $\text{Fe}^{3+}$  sources contribute to total  $\text{Fe}^{3+}$ . The largest  $\text{Cr}(\text{OH})_3$  volume fractions are observed close to both Cr(VI) infiltration zones (Fig. 7c). By contrast, total  $\text{Cr}^{3+}$  concentrations (Fig. 7b) are mainly controlled by the pH dependent solubility of  $\text{Cr}(\text{OH})_3$ . Because  $\text{Cr}(\text{OH})_3$  solubility is higher at lower pH values (Table 3)  $\text{Cr}^{3+}$  concentrations are decreasing with increasing pH values (Fig. 7d). Total  $\text{Fe}^{2+}$  concentrations are not substantially affected by Cr(VI) reduction (Fig. 7g) because  $\text{Fe}^{2+}$  is available in excess of Cr(VI). By analogy to the 1D problem, the  $\text{Fe}^{2+}$  excess over Cr(VI) is inherited from strong kinetic chamosite and annite dissolution (Table 4). Similar to  $\text{Fe}^{2+}$ , steady state total  $\text{SiO}_2$ ,  $\text{Al}^{3+}$ , and  $\text{K}^+$  concentrations (Figs. 7h–j) are controlled by the kinetic dissolution of quartz, annite, and chamosite whereas total  $\text{Ca}^{2+}$  concentrations are controlled by the presence of chromitite in the Cr(VI) infiltration zone (Fig. 7k).

### 5.3.2 Code comparison

Overall, steady state concentrations obtained from different codes match each other well (Fig. 7). However, minor total concentration differences are observable for a few species (e.g.,  $\text{Cr}^{3+}$ ,  $\text{Fe}^{3+}$ ,  $\text{SO}_4^{2-}$ , pH). We suspect that these differences are inherited from minor flow field differences, illustrated with minor differences in the steady state pressure distributions (Fig. 7l). Minor flow field differences are most likely inherited from a different definition of fluid compressibility and a different approach for model discretization. For instance, MIN3P [54] is the only code using grid blocks that are only half the size at the edge of the grid, resulting in a model domain that is 2 m shorter at each of the four grid boundaries when compared to the CRUNCHFLOW [53 and references therein] and TOUGHREACT [51] grid. Moreover, TOUGHREACT is using a pressure and temperature dependent water compressibility that is slightly larger than 0 to solve for fluid pressures, whereas CRUNCHFLOW and MIN3P are using zero water compressibility. CRUNCHFLOW's and MIN3P's use of a zero water compressibility in particular causes a larger pressure for the water injecting grid block when compared to the corresponding TOUGHREACT pressure ( $P_{\text{CRUNCHFLOW}} = 1.010 \times P_{\text{TOUGHREACT}}$ ;  $P_{\text{MIN3P}} = 1.019 \times P_{\text{TOUGHREACT}}$ ), thus inducing a larger pressure gradient across the full model domain in the same order of magnitude. The observation that MIN3P yielded

the largest maximum pressure is inherited from defining water injection for one of the small grid blocks at the model edge. Moreover, this definition shifts the location of water injection by about 2 m for the MIN3P model, which also contributed to the observed pressure gradient differences.

A variable pressure distribution and subsequent varying flow velocities cause varying residence times along specific transport paths, thus introducing total concentration differences for species that are controlled by kinetic mineral dissolution (e.g.,  $\text{Fe}^{2+}$ ,  $\text{SiO}_2$ ,  $\text{Al}^{3+}$ , and pH) (Fig. 7d, g–i). Small pH differences (Fig. 7d) in turn are responsible for minor differences observed for species that are controlled by a pH dependent mineral solubility such as  $\text{SO}_4^{2-}$  and  $\text{Fe}^{3+}$  (jarosite) and  $\text{Cr}^{3+}$  ( $\text{Cr}(\text{OH})_3$ ) (Fig. 7b, e–f).

Despite of minor flow field differences, breakthrough curves for Cr(VI),  $\text{HCO}_3^-$ , and  $\text{K}^+$  match very well (Fig. 8) confirming that, overall, the flow field was wellmatching.

## 5.4 Level #4

### 5.4.1 The fate of individual Cr isotopes

Figure 9a illustrates that the steady state  $\delta^{53}\text{Cr}_{\text{Cr(VI)/SRM979}}$  distribution is not as strongly controlled by the Cr(VI) infiltration zone when compared to the steady state Cr(VI) distribution (Fig. 7a). In particular, maximum  $\delta^{53}\text{Cr}_{\text{Cr(VI)/SRM979}}$  values were obtained for the left hand aquifer boundary (Fig. 2). Large  $\delta^{53}\text{Cr}_{\text{SRM979}}$  values are explained by the minimum pressure gradient and subsequent minimum flow velocities observed for this domain (Fig. 7l). Low velocities in turn increase the aquifer residence time, and thus introduce a larger extent of Cr(VI) reduction along a specific flow path. The different behavior of  $\delta^{53}\text{Cr}_{\text{Cr(VI)/SRM979}}$  and Cr(VI) demonstrates that  $\delta^{53}\text{Cr}$  values are controlled by the extent of Cr(VI) reduction that a particular Cr(VI) load experienced rather than by the total aqueous Cr(VI) concentration [11, 17]. By contrast, Cr(VI) concentrations are controlled by the solubility of a particular Cr(VI)-bearing mineral.

### 5.4.2 Code comparison

Comparing results for problem level #4 demonstrates that the tested codes are capable to accurately simulate the fate of Cr isotopes during the tested processes (fractionation during aqueous kinetic Cr(VI) reduction, non-fractionating precipitation of Cr(III), dissolution of Cr(VI) bearing phase). Most importantly, the steady state  $\delta^{53}\text{Cr}_{\text{SRM979}}$  value distribution for the three Cr pools (e.g., Cr(VI), Cr(III), and precipitated  $\text{Cr}(\text{OH})_3$ ) derived from different codes match almost as good as for the corresponding 1D problem (Fig. 9a–c vs. Fig. 5d). Moreover, the very similar steady

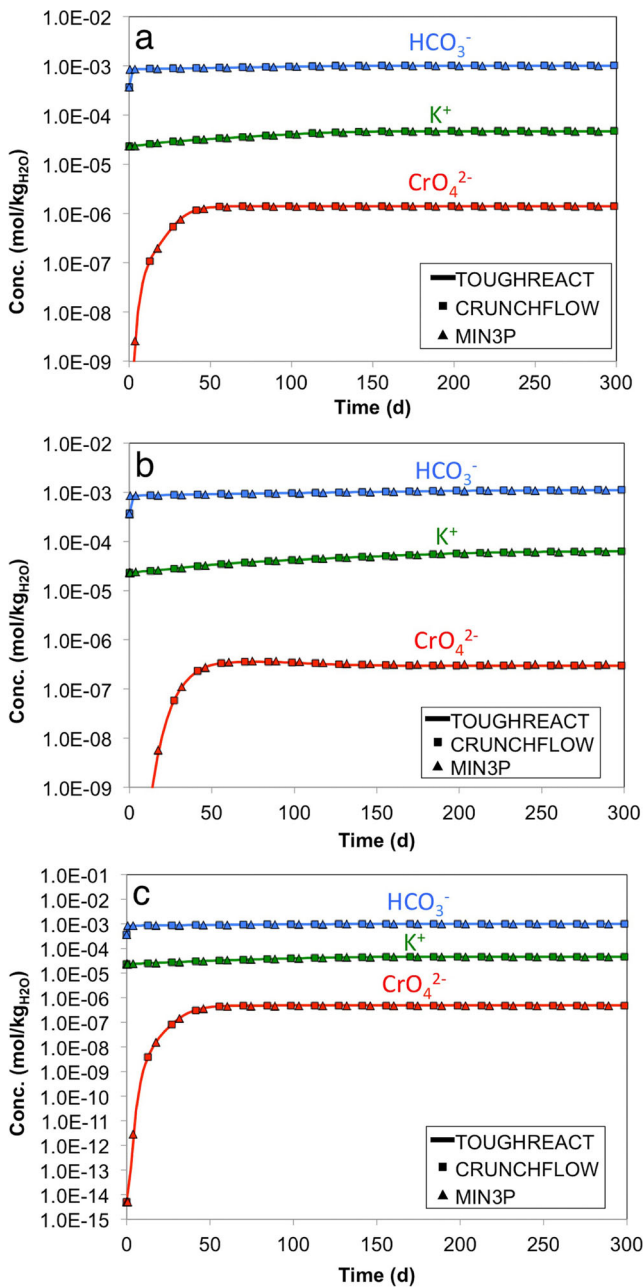


**Fig. 8** CrO<sub>4</sub><sup>2-</sup>, K<sup>+</sup>, and HCO<sub>3</sub><sup>-</sup> breakthrough curves for level #3 observed at (x<sub>20</sub>, y<sub>32</sub>) (a), (x<sub>15</sub>, y<sub>38</sub>) (b), and (x<sub>21</sub>, y<sub>36</sub>) (c)

state  $\delta^{53}\text{Cr}_{\text{Cr}(\text{OH})_3/\text{SRM979}}$  and  $\delta^{53}\text{Cr}_{\text{Cr}^{3+}/\text{SRM979}}$  distributions (Fig. 9b–c) confirm that Cr isotope fractionation was solely simulated during reduction of Cr(VI) to Cr(III), whereas no fractionation occurred during precipitation of Cr(OH)<sub>3</sub>.

Minor differences between MIN3P and the two other codes were obtained for  $\delta^{53}\text{Cr}_{\text{Cr}(\text{OH})_3/\text{SRM979}}$  (Fig. 9c), but only for the left-hand aquifer boundary where the precipitated Cr(OH)<sub>3</sub> volume fractions were very small, on the order of 1e–9 or smaller (Fig. 7c). Accordingly, these minor

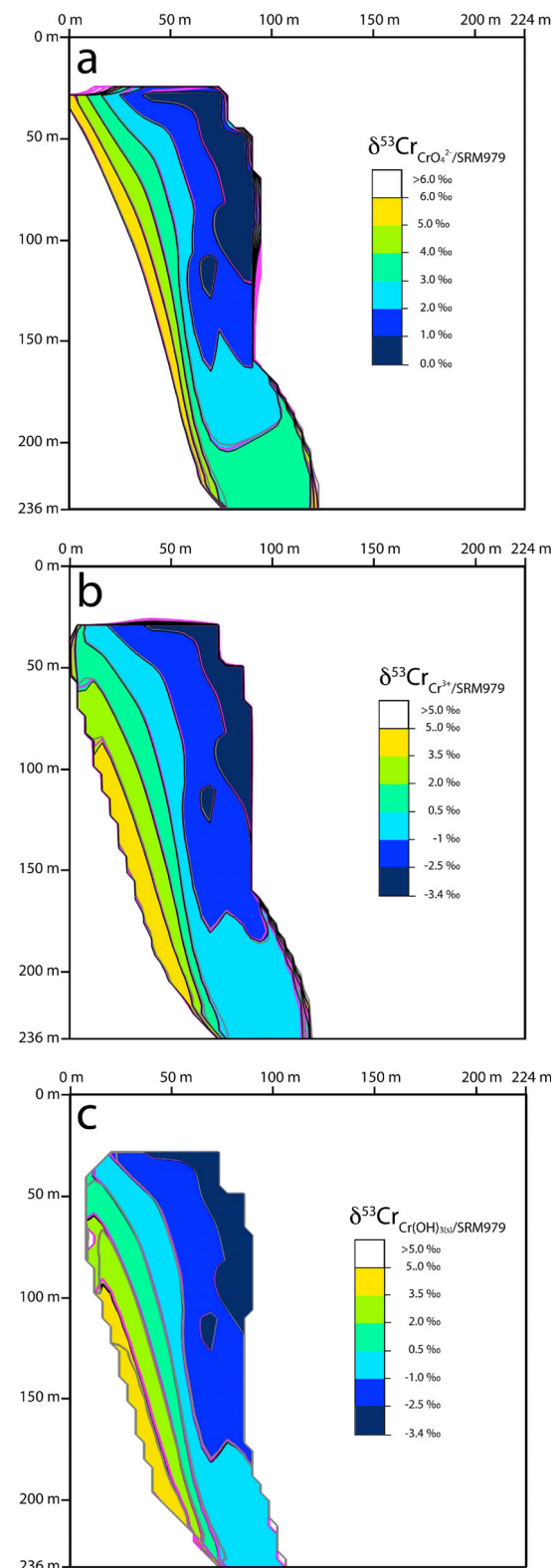


**Fig. 9** Steady state spatial  $\delta^{53}\text{Cr}$  value distribution for the three different Cr pools (Cr(VI), Cr(III), and solid Cr(OH)<sub>3</sub>) obtained for level #4 after a simulated time of 1,000 days. The colors and black contours indicate results obtained from the TOUGHREACT runs. MIN3P and CRUNCHFLOW results are shown as gray and purple contour lines, respectively

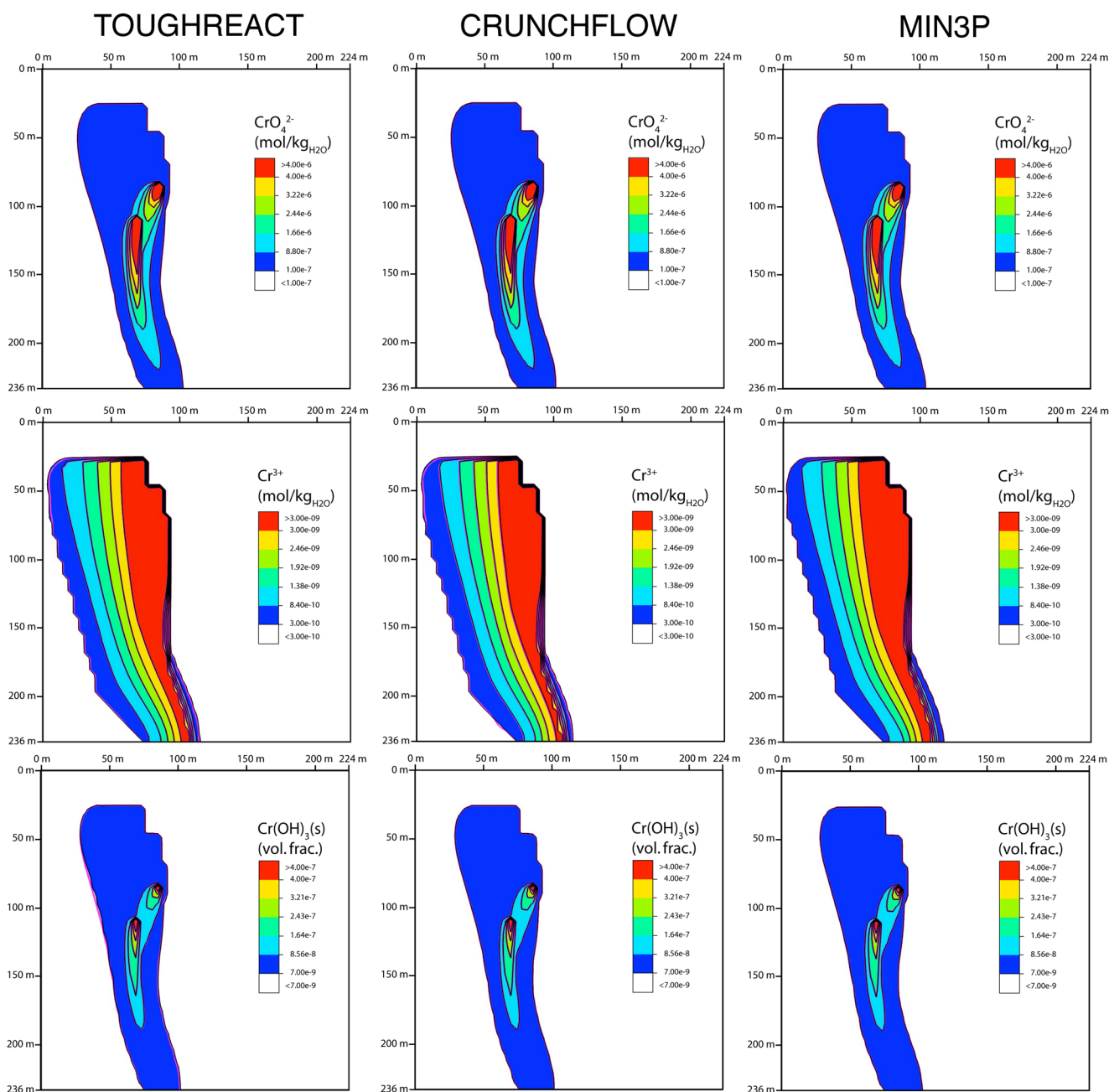


**Fig. 10** Steady state spatial distribution of bulk aqueous Cr(VI) and Cr(III) concentrations and bulk Cr(OH)<sub>3</sub> volume fractions obtained for problem levels #3 and #4 using TOUGHREACT, CRUNCHFLOW, and MIN3P after a simulated time of 1,000 days. The colors and black

contours denote results for level #3, whereas the purple contours refer to the sum of (<sup>52</sup>CrO<sub>4</sub>)<sup>2-</sup> and (<sup>53</sup>CrO<sub>4</sub>)<sup>2-</sup>, (<sup>52</sup>Cr)<sup>3+</sup> and (<sup>53</sup>Cr)<sup>3+</sup> as well as <sup>52</sup>Cr(OH)<sub>3</sub> and <sup>53</sup>Cr(OH)<sub>3</sub> obtained for level #4

differences are attributed to the different approaches of calculating precipitation rates of newly formed minerals. The fact that MIN3P is the only code that is using minimum mineral volume fractions larger than zero means that, for small Cr(OH)<sub>3</sub> volume fractions (on the order of the defined minimum volume fractions),  $\delta^{53}\text{Cr}_{\text{Cr}(\text{OH})_3/\text{SRM979}}$  is affected by the specified minimum <sup>52</sup>Cr(OH)<sub>3</sub> and <sup>53</sup>Cr(OH)<sub>3</sub> volume fractions (8.981529e-11 and 1.018437e-11) corresponding to an initial  $\delta^{53}\text{Cr}_{\text{Cr}(\text{OH})_3/\text{SRM979}}$  of 0.0 ‰.

For larger Cr(OH)<sub>3</sub> volume fractions, MIN3P derived  $\delta^{53}\text{Cr}_{\text{Cr}(\text{OH})_3/\text{SRM979}}$  values are no longer affected by the specified minimum volume fractions such that overall, the different approach of handling secondary mineral phases do not cause major differences and a good overall  $\delta^{53}\text{Cr}_{\text{Cr}(\text{OH})_3/\text{SRM979}$  match was obtained (Fig. 9c).

The observation that, for any of the codes, steady state total concentration distributions obtained for the sum of the Cr(VI) and Cr(III) isotopologues compare almost perfectly

with corresponding total bulk Cr(VI) and Cr(III) concentrations obtained for level #3 (Fig. 10) adds additional confidence to the simulation results. The same applies for the sum of the  $^{52}\text{Cr}(\text{OH})_3$  and  $^{53}\text{Cr}(\text{OH})_3$  end-member volume fractions. The good match between  $\text{Cr}_{\text{total}}$  (problem #3) and  $^{52}\text{Cr} + ^{53}\text{Cr}$  (problem #4) demonstrates that the overall reaction network remained largely unchanged when adding the simulation of Cr isotope fractionation to the 2D problem. Obtaining such a good match is particularly important because in comparison to the 1D problems, the 2D problems also include solid Cr(VI) sources (reactions m3–m6, Table 4), for which  $\log(K)$  adjustments had to be performed to obtain the same bulk Cr(VI) solubility when adding the simulation of individual Cr isotopes to the problem (32–33).

## 6 Summary and conclusion

A benchmark problem set consisting of four problem levels was developed for the simulation of Cr isotope fractionation in 1D and 2D. It was largely adapted from a recent field study where Cr(VI) reduction and accompanying Cr isotope fractionation occurs abiotically by an aqueous reaction with dissolved Fe(II). A first-order reaction rate law with respect to dissolved  $\text{Fe}^{2+}$  was therefore used to simulate Cr(VI) reduction and Cr isotope fractionation. Owing to its low solubility, Cr(III) produced by this aqueous reaction readily precipitated as a  $^{52}\text{Cr}(\text{OH})_3$ – $^{53}\text{Cr}(\text{OH})_3$  solid solution, without additional Cr isotope fractionation. The correct model implementation of Cr isotope fractionation was tested with two 1D problem levels. The first level considered the general flow definition and reaction network only, whereas the second one incorporated the fractionation of Cr isotopes. In addition, two 2D problem levels are provided to ensure the correct model implementation of a solid Cr(VI) source consisting of two different Cr(VI)-bearing mineral phases, which is a typical situation for Cr(VI)-contaminated sites. In analogue to the 1D problem levels, the first 2D level deals with the general flow definition and reaction network, while the Cr isotopic composition of the Cr(VI) source and Cr isotope fractionation was incorporated into the second one.

Correctness of the presented numerical solutions was ensured by running the benchmark problem set with the following four well-established reactive transport modeling codes: TOUGHREACT, MIN3P, CRUNCHFLOW, and FLOTRAN. Results for the 1D Cr isotope fractionation problem were also compared with an analytical Rayleigh-type fractionation model, because it accurately describes Cr isotope fractionation for this first-order irreversible reaction. An additional constraint on the correctness of the results was obtained by comparing results from the problem

levels simulating Cr isotope fractionation with the corresponding ones only simulating bulk concentrations. For all problem levels, model to model comparisons showed excellent agreement, suggesting that for the tested geochemical processes (fractionation during aqueous kinetic Cr(VI) reduction, non-fractionating Cr(III) precipitation, dissolution of Cr(VI)-bearing minerals) all of the tested codes are capable to accurately simulate the fate of individual Cr isotopes.

The presented problem set is proposed to serve as a useful benchmark to test the simulation of stable isotope fractionation during aqueous kinetic as well as mineral precipitation reactions. Modelers seeking to incorporate Cr isotope fractionation, or fractionation of any other isotopic species (e.g., C, Li, S), may therefore find the presented benchmark problem set useful to verify their codes for the geochemical processes tested here. It should be noted, however, that for aqueous kinetic reactions the code-specific simulation approaches were solely tested for first-order reaction kinetics. The two 2D problem levels also provide a base case for code verification that could be expanded by specifying a heterogeneous redox and/or permeability distribution in order to assess the effects of hydrodynamic dispersion and localized Cr(VI) reduction on the resulting Cr isotopic composition. The accurate implementation of such transport effects on the fate of stable isotope ratios, however, should be rigorously tested by future benchmark efforts. The same applies for the accurate simulation of stable isotope fractionation in conjunction with reaction orders other than first-order.

**Acknowledgments** CW was supported by the Subsurface Science Scientific Focus Area funded by the U.S. Department of Energy, Office of Science, Office of Biological and Environmental Research under award number DE-AC02-05CH11231. JD's contribution was funded through a National Science Foundation Division of Earth Sciences Postdoctoral Fellowship under contract number EAR-1144763. RA was funded through an Ontario Research Foundation – Research Excellence Award.

## References

1. Kotas, J., Stasicka, Z.: Chromium occurrence in the environment and methods of its speciation. *Environ. Pollut.* **107**, 263–283 (2000)
2. Oze, C., Bird, D.K., Fendorf, S.: Genesis of hexavalent chromium from natural sources in soil and groundwater. *Proc. Natl. Acad. Sci. U. S. A.* **104**, 6544–6549 (2007)
3. Szalinska, E., Dominik, J., Vignati, D.A.L., Bobrowski, A., Bas, B.: Seasonal transport pattern of chromium(III and VI) in a stream receiving wastewater from tanneries. *Appl. Geochem.* **25**, 116–122 (2010)
4. Rai, D., Sass, B.M., Moore, D.A.: Chromium(III) hydrolysis constants and solubility of chromium(III) hydroxide. *Inorg. Chem.* **26**, 345–349 (1987)

5. Powell, R.M., Puls, R.W., Hightower, S.K., Sabatini, D.A.: Coupled iron corrosion and chromate reduction: mechanisms for subsurface remediation. *Environ. Sci. Technol.* **29**, 1913–1922 (1995)
6. Palmer, C.D., Puls, R.: *W. Iron Metal for Subsurface Remediation; EPA/540/S-94/505; U.S. EPA Ground Water Issue* (1994)
7. Naftz, D.L., Morrison, S.J., Davies, J.A., Fuller, C.C.: *Handbook of Groundwater remediation using permeable reactive barriers.* Elsevier Science, San Diego, USA (2002)
8. Flury, B., Frommer, J., Eggenberger, U., Mäder, U., Nachtegaal, M., Kretzschmar, R.: Assessment of long-term performance and chromate reduction mechanisms in a field scale permeable reactive barrier. *Environ. Sci. Technol.* **43**, 6786–6792 (2009)
9. Wanner, C., Zink, S., Eggenberger, U., Mäder, U.: Assessing the Cr(VI) reduction efficiency of a permeable reactive barrier using Cr isotope measurements and 2D reactive transport modeling. *J. Cotam. Hydrol.* **131**, 54–63 (2012)
10. Faybishenko, B., Hazen, T.C., Long, P.E., Brodie, E.L., Conrad, M.E., Hubbard, S.S., Christensen, J.N., Joyner, D., Borglin, S.E., Chakraborty, R., Williams, K.H., Peterson, J.E., Chen, J., Brown, S.T., Tokunaga, T.K., Wan, J., Firestone, M., Newcomer, D.R., Resch, C.T., Cantrell, K.J., Willett, A., Koenigsberg, S.: In Situ long-term reductive bioimmobilization of Cr(VI) in Groundwater using hydrogen release compound. *Environ. Sci. Technol.* **42**, 8478–8485 (2008)
11. Wanner, C., Zink, S., Eggenberger, U., Mäder, U.: Unraveling the partial failure of a permeable reactive barrier using a multi-tracer experiment and Cr isotope measurements. *Appl. Geochem.* **37**, 125–133 (2013)
12. Zink, S., Schoenberg, R., Staubwasser, M.: Isotopic fractionation and reaction kinetics between Cr(III) and Cr(VI) in aqueous media. *Geochim. Cosmochim. Acta* **74**, 5729–5745 (2010)
13. Basu, A., Johnson, T.M.: Determination of Hexavalent chromium reduction using cr stable isotopes: isotopic fractionation factors for permeable reactive barrier materials. *Environ. Sci. Technol.* **46**, 5353–5360 (2012)
14. Kitchen, J.W., Johnson, T.M., Bullen, T.D., Zhu, J., Raddatz, A.L.: Chromium isotope fractionation factors for reduction of Cr(VI) by aqueous Fe(II) and organic molecules. *Geochim. Cosmochim. Acta* (2012)
15. Jamieson-Hanes, J.H., Gibson, B.D., Lindsay, M.B.J., Kim, Y., Ptacek, C.J., Blowes, D.W.: Chromium Isotope fractionation during reduction of cr(vi) under saturated flow conditions. *Environ. Sci. Technol.* **46**, 6783–6789 (2012)
16. Izbicki, J.A., Ball, J.W., Bullen, T.D., Sutley, S.J.: Chromium, chromium isotopes and selected trace elements, western Mojave Desert, USA. *Appl. Geochem.* **23**, 1325–1352 (2008)
17. Berna, E.C., Johnson, T.M., Makdisi, R.S., Basu, A.: Cr stable isotopes as indicators of Cr(VI) reduction in groundwater: a detailed time-series study of a point-source plume. *Environ. Sci. Technol.* **44**, 1043–1048 (2010)
18. Wanner, C., Eggenberger, U., Kurz, D., Zink, S., Mäder, U.: A chromate-contaminated site in southern Switzerland, part 1: site characterization and the use of Cr isotopes to delineate fate and transport. *Appl. Geochem.* **27**, 644–654 (2012)
19. Izbicki, J.A., Bullen, T.D., Martin, P., Schroth, B.: Delta Chromium-53/52 isotopic composition of native and contaminated groundwater, Mojave Desert, USA. *Appl. Geochem.* **27**, 841–853 (2012)
20. Ellis, A.S., Johnson, T.M., Bullen, T.D.: Chromium isotopes and the fate of hexavalent chromium in the environment. *Science* **295**, 2060–2062 (2002)
21. Wanner, C., Sonnenthal, E.L.: Assessing the control on the effective kinetic Cr isotope fractionation factor: a reactive transport modeling approach. *Chem. Geol.* **337**, 88–98 (2013)
22. Dossing, L.N., Dideriksen, K., Stipp, S.L.S., Frei, R.: Reduction of hexavalent chromium by ferrous iron: a process of chromium isotope fractionation and its relevance to natural environments. *Chem. Geol.* **285**, 157–166 (2011)
23. Sikora, E.R., Johnson, T.M., Bullen, T.D.: Microbial mass-dependent fractionation of chromium isotopes. *Geochim. Cosmochim. Acta* **72**, 3631–3641 (2008)
24. DePaolo, D.J.: Surface kinetic model for isotopic and trace element fractionation during precipitation of calcite from aqueous solutions. *Geochim. Cosmochim. Acta* **75**, 1039–1056 (2011)
25. Druhan, J.L., Steefel, C.I., Williams, K.H., DePaolo, D.J.: Calcium isotope fractionation in groundwater: molecular scale processes influencing field scale behavior. *Geochim. Cosmochim. Acta* **119**, 93–116 (2013)
26. Green, C.T., Bohlke, J.K., Bekins, B.A., Phillips, S.P.: Mixing effects on apparent reaction rates and isotope fractionation during denitrification in a heterogeneous aquifer. *Water Resour. Res.* **46**, W08525 (2010). doi:10.1029/2009WR008903
27. Abe, Y., Hunkeler, D.: Does the Rayleigh equation apply to evaluate field isotope data in contaminant hydrogeology? *Environ. Sci. Technol.* **40**, 1588–1596 (2006)
28. Van Breukelen, B.M.V., Prommer, H.: Beyond the Rayleigh Equation: reactive transport modeling of isotope fractionation effects to improve quantification of biodegradation. *Environ. Sci. Technol.* **42**, 2457–2463 (2008)
29. Jamieson-Hanes, J.H., Amos, R.T., Blowes, D.W.: Reactive Transport modeling of chromium isotope fractionation during Cr(VI) reduction. *Environ. Sci. Technol.* **46**, 13311–13316 (2012)
30. Wanner, C., Eggenberger, U., Mäder, U.: A chromate-contaminated site in southern Switzerland, part 2: reactive transport modeling to optimize remediation options. *Appl. Geochem.* **27**, 655–662 (2012)
31. Druhan, J.L., Steefel, C.I., Molins, S., Williams, K.H., Conrad, M.E., DePaolo, D.J.: Timing the onset of sulfate reduction over multiple subsurface acetate amendments by measurement and modeling of sulfur isotope fractionation. *Environ. Sci. Technol.* **46**, 8895–8902 (2012)
32. Druhan, J.L., Steefel, C.I., Conrad, M.E., DePaolo, D.J.: A large column analog experiment of stable isotope variations during reactive transport: I. A Comprehensive model of sulfur cycling and  $\delta^{34}\text{S}$  fractionation. *Geochim. Cosmochim. Acta* **124**, 366–393 (2014)
33. Zhang, Y.-C., Prommer, H., Broers, H.P., Slomp, C.P., Greskoviak, J., Van der Grift, B., Van Cappellen, P.: Model-Based integration and analysis of biogeochemical and isotopic dynamics in a nitrate-polluted pyritic aquifer. *Environ. Sci. Technol.* **47**, 10415–10422 (2013)
34. Gibson, B.D., Amos, R.T., Blowes, D.W.:  $(^{29}\text{S}/^{27}\text{S})$  fractionation during sulfate reduction in groundwater treatment systems: reactive transport modeling. *Environ. Sci. Technol.* **45**, 2863–2870 (2011)
35. Van Breukelen, B.M., Griffioen, J., Røling, W.F.M., van Verseveld, H.W.: Reactive transport modelling of biogeochemical processes and carbon isotope geochemistry inside a landfill leachate plume. *J. Cotam. Hydrol.* **70**, 249–269 (2004)
36. Van Breukelen, B.M., Hunkeler, D., Volkering, F.: Quantification of sequential chlorinated ethene degradation by use of a reactive transport model incorporating isotope fractionation. *Environ. Sci. Technol.* **39**, 4189–4197 (2005)
37. Atteia, O., Franceschi, M., Dupuy, A.: Validation of reactive model assumptions with isotope data: application to the Dover case. *Environ. Sci. Technol.* **42**, 3289–3295 (2008)

38. Prommer, H., Aziz, L.H., Bolano, N., Taubald, H., Schueth, C.: Modelling of geochemical and isotopic changes in a column experiment for degradation of TCE by zero-valent iron. *J. Cotam. Hydrol.* **97**, 13–26 (2008)
39. Pooley, K.E., Blessing, M., Schmidt, T.C., Haderlein, S.B., Macquarrie, K.T.B., Prommer, H.: Aerobic biodegradation of chlorinated ethenes in a fractured bedrock aquifer: quantitative assessment by compound-specific isotope analysis (CSIA) and reactive transport modeling. *Environ. Sci. Technol.* **43**, 7458–7464 (2009)
40. Rolle, M., Chiogna, G., Bauer, R., Griebler, C., Grathwohl, P.: Isotopic Fractionation by transverse dispersion: flow-through microcosms and reactive transport modeling study. *Environ. Sci. Technol.* **44**, 6167–6173 (2010)
41. Steefel, C.I., Appelo, C.A.J., Arora, B., Jacques, D., Kalbacher, T., Kolditz, O., Lagneau, V., Lichtner, P.C., Mayer, K.U., Meussen, H., Molins, S., Moulton, D., Parkhurst, D.L., Shao, H., Simunek, J., Spycher, N., Yabusaki, S., Yeh, G.T.: Reactive transport codes for subsurface environmental simulation. *Computational Geoscience* (2014)
42. Schoenberg, R., Zink, S., Staubwasser, M., von Blanckenburg, F.: The stable Cr isotope inventory of solid earth reservoirs determined by double spike MC-ICP-MS. *Chem. Geol.* **249**, 294–306 (2008)
43. Ellis, A.S., Johnson, T.M., Bullen, T.D.: Using chromium stable isotope ratios to quantify Cr(VI) reduction: lack of sorption effects. *Environ. Sci. Technol.* **38**, 3604–3607 (2004)
44. Johnson, J.W., Oelkers, E.H., Helgeson, H.C.: SUPCRT92: a software package for calculating the standard molal thermodynamic properties of minerals, gases, aqueous species, and reactions from 1 to 5000 bar and 0 to 1000°C. *Comput. Geosci.* **18**, 899–948 (1992)
45. Wolery, T.J.: EQ3/6: Software package for geochemical modeling of aqueous systems: package overview and installation guide (version 7.0). Livermore, California (1992)
46. Ball, J.W., Nordstrom, D.K.: Critical evaluation and selection of standard state thermodynamic properties for chromium metal and its aqueous ions, hydrolysis species, oxides, and hydroxides. *J. Chem. Eng. Data* **43**, 895–918 (1998)
47. Lasaga, A.C.: Chemical kinetics of water-rock interactions. *J. Geoph. Res.* **89**, 4009–4025 (1984)
48. Buerge, I.J., Hug, S.J.: Kinetics and pH dependence of chromium(VI) reduction by iron(II). *Environ. Sci. Technol.* **31**, 1426–1432 (1997)
49. Shields, W.R., Murphy, T.J., E. J., C., Garner, E.L.: Absolute isotopic abundance ratios and atomic weight of a reference sample of chromium. *J. Res. Natl. Bur. Stand. Sect. Phys. Chem. A* **70**, 193 (1966)
50. Coplen, T.B.: Guidelines and recommended terms for expression of stable-isotope-ratio and gas-ratio measurement results. *Rapid Commun. Mass Spectrom.* **25**, 2538–2560 (2011)
51. Xu, T., Spycher, N., Sonnenthal, E.L., Zhang, G., Zheng, L., Pruess, K.: TOUGHREACT Version 2.0: a simulator for subsurface reactive transport under non-isothermal multiphase flow conditions. *Comput. Geosci.* **37**, 763–774 (2011)
52. Lichtner, P.C.: FLOTRAN users manual: two-phase non-isothermal coupled thermal-hydrologic-chemical (THC) reactive flow and transport code version 2. Los Alamos National Laboratory, New Mexico, USA (2007)
53. Steefel, C., Maher, K.: Fluid-rock interaction: a reactive transport approach. In: Oelkers, E.H., Schott, J. (eds.) *Thermodynamics and Kinetics of Water-Rock Interaction*. Mineralogical Society of America: 2009, Reviews in Mineralogy, vol. 70, pp. 485–532
54. Mayer, K.U., Frind, E.O., Blowes, D.W.: Multicomponent reactive transport modeling in variably saturated porous media using a generalized formulation for kinetically controlled reactions. *Water Resour. Res.* **38**, 1174 (2002). doi:[10.1029/2001WR000862](https://doi.org/10.1029/2001WR000862)
55. Baron, D., Palmer, C.D.: Solubility of  $\text{KFe}_3(\text{CrO}_4)_2(\text{OH})_6$  at 4 to 35°C. *Geochim. Cosmochim. Acta* **60**, 3815–3824 (1996)
56. Palandri, J.L., Kharaka, Y.K.A.: Compilation of rate parameters of water-mineral interaction kinetics for application to geochemical modeling. U.S. Geological Survey Open-File Report 2004-1068; US Geological Survey (2004)
57. Appelo, C.A.J., Postma, D.: *Geochemistry, groundwater and pollution*, 2nd edn. Balkema, Amsterdam, The Netherlands (2005)